

Enhancing Event Reconstruction in SuperCDMS through Handling Correlated Frequencies in Noise

by

Tobias Faehndrich

A THESIS SUBMITTED IN PARTIAL FULFILLMENT OF
THE REQUIREMENTS FOR THE DEGREE OF

BACHELOR OF SCIENCE

in

The Faculty of Science

(Physics and Astronomy)

THE UNIVERSITY OF BRITISH COLUMBIA

(Vancouver)

April 2024

© Tobias Faehndrich 2024

The following individuals certify that they have read, and recommend to the Faculty of Science for acceptance, the thesis entitled:

Enhancing Event Reconstruction in SuperCDMS through Handling Correlated Frequencies in Noise

submitted by **Tobias Faehnrich** in partial fulfillment of the requirements for the degree of
Bachelor of Science in Physics

Examining Committee:

Supervisor: Dr. Scott Oser

Additional Examiner: Dr. Yan Liu

Abstract

In the Super Cryogenic Dark Matter Search experiment, we leverage optimal filter techniques to reconstruct the energies deposited by particle interactions within the detector. The currently used optimal filter method assumes uncorrelated frequencies in noise, deviating from the reality of correlated frequencies. Neglecting correlated noise worsens energy resolution, limiting the ability of the experiment to distinguish candidate dark matter events from background events. This thesis establishes a novel cluster sort optimal filter method. This approach is shown to improve the energy resolution from the traditional diagonal approximation method under both simulated and real noise conditions examined in this work. It additionally, outperforms the full inversion method both in computational speed and precision. These findings not only advance our understanding of optimal filter techniques but also hold promise for improving the sensitivity and accuracy of dark matter detection experiments.

Lay Summary

In the Super Cryogenic Dark Matter Search experiment, a computational analysis technique called the optimal filter is used to determine the energy that particles leave in our detector. The current method used to analyze these signals simplifies the computation by assuming simple noise. This oversimplification could make it much harder to distinguish between real dark matter signals and other background events. This thesis develops a new method called the cluster sort optimal filter, which better accounts for cases where the noise is complicated. This work not only deepens our knowledge of signal processing techniques but also brings us closer to making more accurate and sensitive dark matter detection experiments.

Preface

The content of this thesis is original unpublished work by the author. The idea for this study came about through discussions with the author's supervisors, Dr. Scott Oser and Dr. Yan Liu. All necessary python scripts, as well as the resulting plots and data were created by the author unless otherwise noted. Individual techniques and methods used but not developed by the author have been cited where appropriate.

Table of Contents

Abstract	ii
Lay Summary	iii
Preface	iv
Table of Contents	v
List of Figures	vii
Acknowledgements	ix
1 Dark Matter Introduction	1
1.1 Motivation	1
1.1.1 Galaxy Velocities	1
1.1.2 Flat rotation curves	1
1.1.3 Gravitational Lensing	1
1.1.4 The Cosmic Microwave Background	3
1.1.5 Big Bang Nucleosynthesis	3
1.2 Dark Matter Candidates	4
1.2.1 Weakly-Interacting Massive Particles	4
1.2.2 Dark Sector	5
1.2.3 Axions and Axion-like Particles	5
1.3 Dark Matter Detection	5
1.3.1 Direct Detection	5
1.3.2 Indirect Detection	8
1.3.3 Production	8
1.4 SuperCDMS	8
1.4.1 SNOLAB	8
1.4.2 Detector Mechanisms	8
2 Energy Reconstruction	13
2.1 Traditional Optimal Filter	13
2.2 Computational Underpinnings	15
3 Correlation Clustering Optimal Filter	18
3.1 Non-Stationary Noise	18
3.1.1 Non-diagonal Correlation Matrix Example	18
3.1.2 Matrix Inversion Complexity and Condition Number	18
3.2 Cluster Sort Method	19
3.2.1 Novel Optimal Filter Application	19

Table of Contents

3.2.2	Correlation Clustering	20
3.3	Covariance Sorting with Cluster Mapping and Remapping	21
4	Results and Discussion	24
4.1	Analysis Approach	24
4.2	Simulated Non-Stationary Noise	24
4.3	Down-sampled Real Noise	25
4.4	Varying Analysis Parameters	28
4.5	Interpreting Results	30
5	Conclusion	31
5.1	Performance of Correlation Clustering	31
5.2	Future Work	31
	Bibliography	32

List of Figures

1.1	The M33 rotation curve (points) compared with the best-fit model (continuous line). The expected rotation velocity based on the stellar disk contribution is represented by the short dashed line. The differences between observed data points and the prediction from the stellar disk can be accounted for with a dark matter halo model. Adapted from Ref [1].	2
1.2	The Bullet Cluster (1E 0657-56) shows the result of a collision between two galaxies. The composite image (from Ref [2]) has an optical image as the background, which contains the typical orange and white coloured galaxies (and stars) in and around the cluster. Overlayed in pink is an X-ray image of the hot gas, which makes up the majority of the baryonic (consisting of atoms) mass in the cluster. The matter distribution in the cluster is determined through weak gravitational lensing and is shown in blue. The discrepancy between where the matter is distributed and where the hot gas is located provides strong evidence that much of the matter is dark and collisionless.	3
1.3	The Planck (Ref [3]) CMB map of anisotropies (a) and associated Planck 2018 temperature power spectrum that is well fitted to the Λ CDM model (b). The lower panel of (b) shows residuals with uncertainties that remain within $\pm 1\sigma$	4
1.4	A schematic of the 3 possible detection methods. Dark matter is represented by the χ and a generic standard model particle is represented by the abbreviation SM. The centre circle represents the interaction. The figure was taken from Ref [4].	6
1.5	The three main direct detection signal types with some examples of experiments that are sensitive to the effects. Figure taken from [5].	7
1.6	The SuperCDMS experimental schematic. Taken from the SuperCDMS collaboration paper [6].	9
1.7	Schematic representation of energy recoil in a SuperCDMS detector (upper). The recoil creates lattice vibrations (phonons) that get captured by sensors on the face of the detector. An example trace of the digitized energy is shown (lower). Adapted from [7].	10
1.8	QET detector mechanism schematic. Figure put together with sub-figures from the SuperCDMS collaboration.	11
1.9	The projected dark matter sensitivities for the SuperCDMS SNOLAB run. Taken from the SuperCDMS collaboration paper [6].	12
2.1	An example energy spectrum (a) after a run, with each part of the energy spectrum accounted for by various known background signal distributions (taken from [6]). An example of the theoretical exponential dark matter energy distribution (b) signature based on the cross-section and mass of the dark matter (taken from SuperCDMS collaboration member, Jodi Cooley at SMU).	14

2.2	Example case from SuperCDMS (Ref [8]) with the left plot showing the signal ($S(t) = a \cdot A(t) + n(t)$) and the right plot showing the fit ($a \cdot A(t)$)	14
3.1	An example of a simple colour map plot showing the correlation matrix for the real component of 1000 of the noise frequency bins. Noise taken from SuperCDMS.	19
3.2	A simplified schematic of the three OF methods, focusing on the construction of the inverse covariance matrix (simplified to the inverse correlation matrix in this diagram). The cluster sort method is shown to preserve the large off-diagonal terms that the diagonal method ignores.	21
3.3	A simple clustering example with a 10x10 matrix. Dark blue values represent large correlations and dark red values represent no correlation. The index clusters are used to rearrange the indices to be block diagonal in the right subplot.	23
4.1	The left-most subplot shows an example of the simulated time series noise. The middle subplot is the scaled pulse template. The right-most subplot is the addition of the two other subplots.	25
4.2	The simulated noise amplitude estimate results distribution is plotted in a histogram. The three methods are each applied on 1000 pulses. The standard deviation of each method is denoted in the legend.	26
4.3	Real down-sampled time series noise and composite event example.	26
4.4	The real down-sampled noise amplitude estimate results distribution is plotted in a histogram. The three methods are each applied on 1000 pulses. The standard deviation of each method is denoted in the legend.	27
4.5	Effect of varying cluster correlation threshold on method performance. The optimal threshold for this noise is found to be 0.3.	28
4.6	Effect of varying number of bins per trace on method performance. Lowering the number of bins reduces inversion errors in the full method while providing more information about frequencies in the noise improves performance in the diagonal and sorting methods.	29
4.7	Effect of varying amplitude scale on template on method performance. The original results remain consistent regardless of whether the template dominates or is buried by the noise.	29
4.8	Effect of varying number of traces on method performance. Increasing the number of traces improves the performance of the full method, while the sorting method is outperformed by the diagonal method with a minimal number of traces.	30

Acknowledgements

I would like to thank my supervisors, Dr. Scott Oser and Dr. Yan Liu, for their tremendous support and guidance throughout the past year of this thesis project. They both provided me with a place to learn and ask questions and for that, I am indebted to them.

I am grateful for all the friends I have had the honour to meet in the Physics and Astronomy department at UBC. Their curiosity and drive inspire me every day.

I also want to thank my family for their continuous love and support throughout my life and for being willing to listen to me practice my thesis presentation a dozen times over the Easter long weekend.

I extend my deepest gratitude to my dear Anna for her unwavering support and invaluable feedback throughout the duration of this thesis. She has been a constant source of strength during the ups and downs of this project.

SDG.

Chapter 1

Dark Matter Introduction

1.1 Motivation

Contemporary observations of the cosmic microwave background (CMB), notably from NASA's Wilkinson Microwave Anisotropy Probe (WMAP) [9] and more recently, the European Space Agency's (ESA) Planck mission [3], strongly align with the standard model of cosmology, known as the Λ CDM (Lambda cold dark matter) model. In this framework, dark matter and dark energy collectively constitute approximately 95% of the universe's total mass-energy content. Dark matter alone constitutes 26.8% of the mass-energy content, encompassing 85% of the universe's mass. Thus it has emerged as a central focus in the realms of astrophysics and cosmology, giving rise to an entire field of research.

1.1.1 Galaxy Velocities

In 1933, the Swiss astrophysicist Fritz Zwicky used measurements of the luminous matter within the Coma Cluster in conjunction with the virial theorem to study its characteristics [10]. Based on the unexpectedly large Doppler shift in the galaxies' velocities, Zwicky proposed that the cluster's density was far greater than what could be accounted for by visible matter alone. This work provided strong initial evidence that there is a significant presence of unseen matter within galaxy clusters. It is also where the term 'dunkel-Materie' or 'dark matter' was coined.

1.1.2 Flat rotation curves

From the mid-70s to early 80s, Vera Rubin with Kent Ford and Norbert Thonnard, published convincing observations of several spiral galaxies, which showcased anomalous 'flat' rotation curves [11, 12]. The results did not follow the expectation that stars farther out from the central bulge of the galaxy (where most of the luminous mass was found), would orbit more slowly (following Kepler's Law). Their conclusion was once again that invisible matter extends beyond the visible galaxy. The Andromeda Galaxy (M33) was further investigated by Corbelli et al. to better understand its distribution of dark matter and it was found to agree with the theoretical descriptions of the so-called 'hierarchical clustering Cold Dark Matter models' (namely, Λ CDM) [1]. Figure 1.1 illustrates this data, showcasing the impact of dark matter on galactic dynamics.

1.1.3 Gravitational Lensing

Strong evidence for dark matter was further found [13, 14] from the optical and x-ray emission of the stars and hot gas respectively within the Bullet Cluster (1E 0657-56). Gravitational lensing of the background objects was used to show the gravitational field of the cluster and was compared to the positions of the stars and gas. The results defied the non-dark matter expectation that the gravitational potential would closely follow the distribution of the more massive and collisional hot gas. Instead, it affirmed the collisionless nature of dark matter within

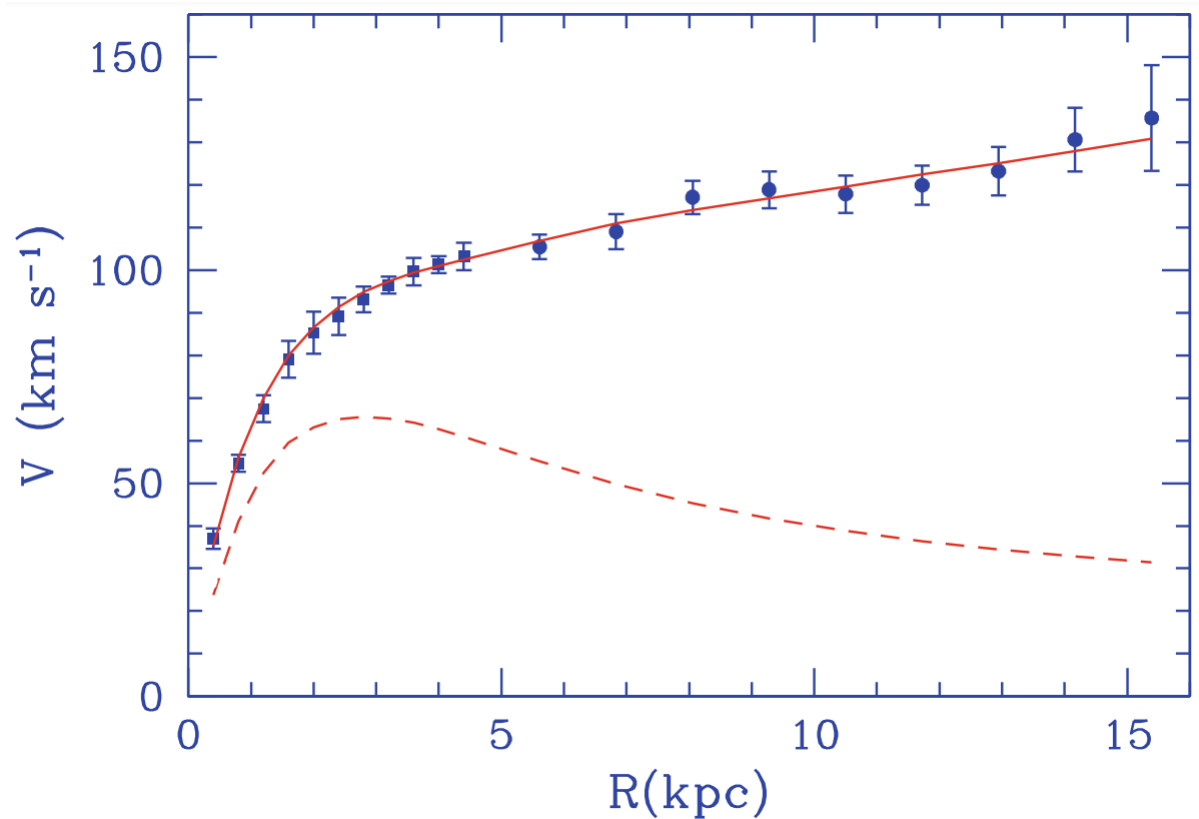


Figure 1.1: The M33 rotation curve (points) compared with the best-fit model (continuous line). The expected rotation velocity based on the stellar disk contribution is represented by the short dashed line. The differences between observed data points and the prediction from the stellar disk can be accounted for with a dark matter halo model. Adapted from Ref [1].



Figure 1.2: The Bullet Cluster (1E 0657-56) shows the result of a collision between two galaxies. The composite image (from Ref [2]) has an optical image as the background, which contains the typical orange and white coloured galaxies (and stars) in and around the cluster. Overlayed in pink is an X-ray image of the hot gas, which makes up the majority of the baryonic (consisting of atoms) mass in the cluster. The matter distribution in the cluster is determined through weak gravitational lensing and is shown in blue. The discrepancy between where the matter is distributed and where the hot gas is located provides strong evidence that much of the matter is dark and collisionless.

the galaxies. A striking visual of this is shown in the Chandra X-ray Observatory composite image [2] as shown in figure 1.2.

1.1.4 The Cosmic Microwave Background

Finally, the power spectrum of small temperature fluctuations in the CMB has been well fitted with the Λ CDM model (to the exclusion of other models) by WMAP [9] and Planck [3], which additionally affirms the existence of dark matter.

1.1.5 Big Bang Nucleosynthesis

In addition to the evidence listed thus far, large-scale structures and big-bang nucleosynthesis (BBN) have constrained the properties of dark matter and thus help indicate which candidates are the most promising. More specifically, on top of being ‘dark’, the BBN suggests [15] that

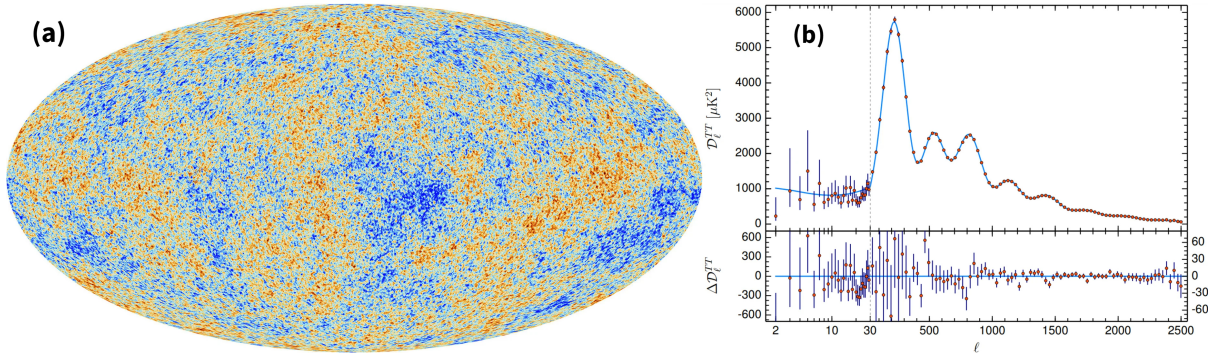


Figure 1.3: The Planck (Ref [3]) CMB map of anisotropies (a) and associated Planck 2018 temperature power spectrum that is well fitted to the ΛCDM model (b). The lower panel of (b) shows residuals with uncertainties that remain within $\pm 1\sigma$.

dark matter is non-baryonic (i.e. not made up of atoms), in order to reconcile the discrepancy between the total cosmological density of matter and the density of baryonic matter which ultimately set in place the abundance of light elements such as deuterium that we see in the universe today. This means that dark matter is not just dust or cold gas that we cannot see.

1.2 Dark Matter Candidates

Despite the compelling evidence for the existence of dark matter, its composition remains elusive. Over the past several decades, numerous candidates have been proposed in attempts to describe the cosmological observations accurately. From the Standard Model (SM) of particle physics, we have one particle that has mass, is neutrally charged and is stable; namely the neutrino. It turns out that the neutrino's mass is too small to make up the required mass content of the universe [16] and the relativistic nature of the neutrino is inconsistent with early universe observations, which requires that dark matter be ‘cold’, i.e. non-relativistic. Thus, it is widely thought that dark matter is some kind of new particle outside of the SM of particle physics. In the following sections, I will provide brief descriptions of some of the most commonly discussed candidates.

1.2.1 Weakly-Interacting Massive Particles

Weakly Interacting Massive Particles (WIMPs) quickly emerged as a leading dark matter candidate over the past few decades. WIMPs hold the potential to explain the observed large-scale structure of the universe. If they were produced in thermal equilibrium during the early universe, WIMPs would have been in a cycle of creation and annihilation until the expansion rate of the universe got larger than the annihilation rate, which would have led to a state of “freeze-out,” (no longer in thermal equilibrium). The so-called relic density of WIMPs post-freeze-out depends on their annihilation cross-sections, which turns out to be on the order of the weak scale [16, 17]. Independently from cosmological predictions, theoretical extensions of the SM, such as Supersymmetry (SUSY) and universal extra dimensions, predict the existence of particles, such as the neutralino and Kaluza-Klein particles, which could manifest as WIMPs [18]. Although WIMPs were originally associated with supersymmetry, the definition of WIMPs has broadened to encompass any massive particle exhibiting generically weak interactions with regular matter. The convergence of cosmological and particle physics principles has offered WIMPs

strong support.

1.2.2 Dark Sector

The Dark Sector of particles is a theorized class of particles that interact minimally with regular matter. The theory suggests a so-called “dark-charge” which is the dark sector’s analogy to electric charge and with which a dark photon could exist. The dark photon would similarly be a force carrier and also have the same quantum numbers as the SM photon, but would have mass [19]. The dark photon is expected to have some kinetic mixing with the SM photon which leads to the possibility of the dark sectors detection. Experiments such as Belle-II [20] and DarkLight [21] aim to search for DM candidates within the dark sector.

1.2.3 Axions and Axion-like Particles

A charge-parity (CP) violation shows up in quantum chromodynamics which would lead to (amongst other things), the neutron having a non-zero electric dipole moment [22]. Efforts to measure an electric dipole moment in the neutron have been unsuccessful. In response to this so-called “strong CP problem”, theorists proposed a solution via a new spontaneous U(1) symmetry-breaking which would come along with an associated particle, named the axion [16, 23]. If axions exist, they would need to be extremely light and have a very small interaction cross-section with regular matter. They could have been abundantly produced non-thermally in a phase transition in the early universe, and depending on their specific properties produce the observed dark matter signatures [24]. Several experiments search for generic axions, and one experiment, the Axion Dark Matter Experiment (ADMX) specifically searches for dark matter axions [25–27]. Other extensions of the SM also propose more general axion-like particles (ALPs) which similarly are associated with a spontaneously broken U(1) symmetry but with less constrained mass and coupling strength. Thus, several WIMP and light dark matter (LDM) experiments additionally probe for ALPs in the eV - keV range via the axioelectric effect [28].

1.3 Dark Matter Detection

Dark matter experiments can be grouped into three main detection methods (see Figure 1.4), consisting of direct detection, indirect detection and production via colliders. In the following sub-sections I will discuss the central ideas for these detection methods.

1.3.1 Direct Detection

Direct detection experiments aim to measure rare elastic recoil collisions of DM with SM targets. The Earth moves around and along with the solar system, through our local Milky Way galaxy and thus the dark matter halo (which is additionally assumed to have a Maxwell-Boltzmann velocity distribution). This results in a “dark matter wind” that continually hits the earth and the terrestrial DM experiments. The small cross-section of the dark matter would determine the expected rate of interaction in detectors. The amount of deposited energy can be determined based on the target mass and the DM mass, as well as the relative speed of the DM, and the scattering angle.

The DM-SM cross-section is thought to be extremely small, which poses a challenge when trying to search for DM on top of all the background (non-DM) events. To maximize the effectiveness of the detectors, experiments put extensive work into shielding from as many

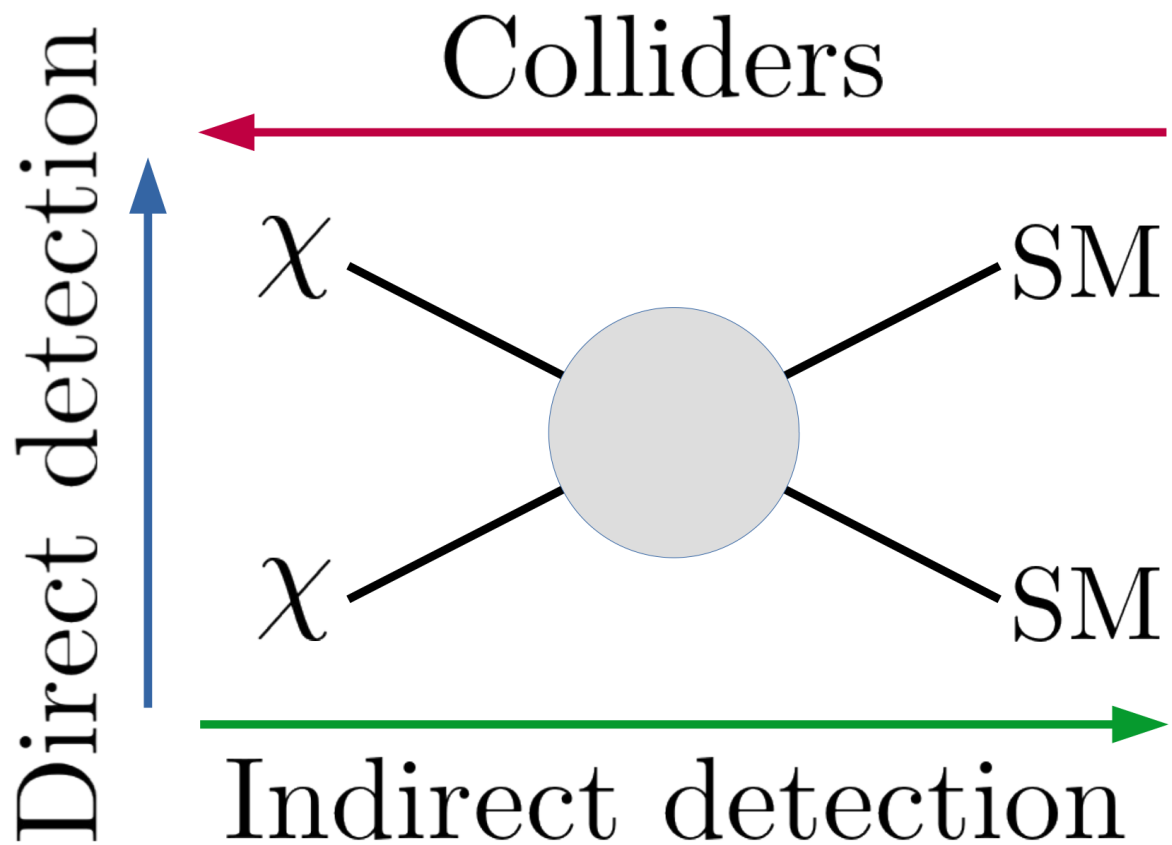


Figure 1.4: A schematic of the 3 possible detection methods. Dark matter is represented by the χ and a generic standard model particle is represented by the abbreviation SM. The centre circle represents the interaction. The figure was taken from Ref [4].

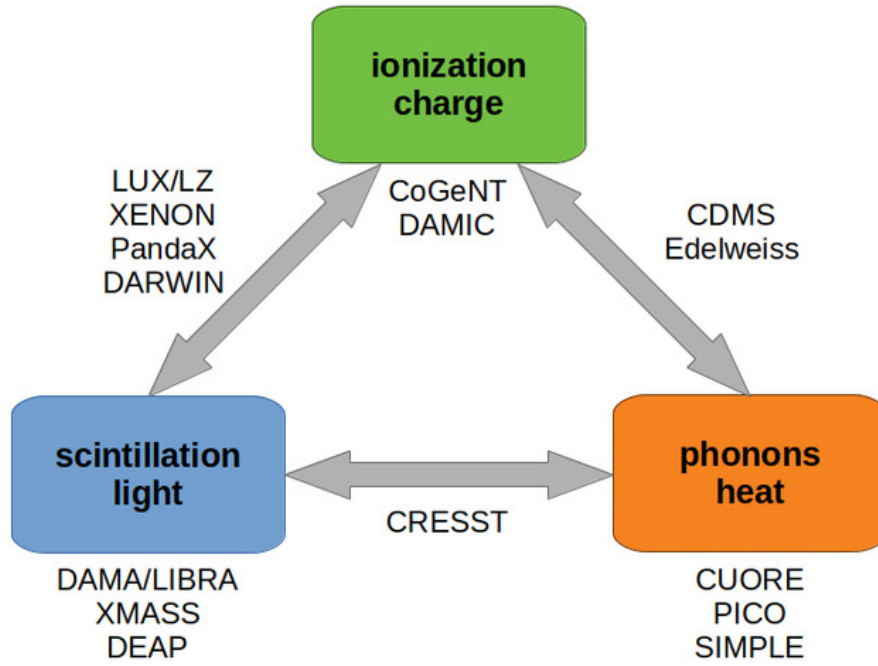


Figure 1.5: The three main direct detection signal types with some examples of experiments that are sensitive to the effects. Figure taken from [5].

background events as possible. This is achieved by placing detectors deep underground to shield from large amounts of cosmic radiation at the surface of the earth, as well as by using shielding materials such as lead (for gamma rays) or water (for neutrons) to shield from radioactive decays, which can originate from within the laboratory environment. They additionally maximize the total detector target mass and measurement time to increase the probability of measuring dark matter recoil events. Finally, they require precise and accurate energy resolution, so that the resulting energy spectrums of measured events can be confidently used to determine if DM was measured or not.

Direct dark matter searches can look for either electron or nuclear recoils, which produce slightly different ionization-to-energy signatures. The standard WIMP DM would recoil off of the nucleus, so being able to discriminate between the types of recoils can improve the sensitivity of an experiment by simply doing a cut on all the electron-recoil events (coming from backgrounds). Other DM candidates could also recoil off of electrons and so being able to measure these smaller signals is also of importance for these experiments.

Direct dark matter experiments are typically sensitive to either detector lattice vibrations (phonons) which get converted to heat, charge (ionization), scintillation light (photons), or a combination of these (which is what often allows for recoil discrimination). Figure 1.5 shows a schematic triangle of these direct detection types with some of the different experiments from around the world. These signal types are typically measured with ionization-based detectors (such as IGEX [29] and CoGeNT [30]), room-temperature scintillators (such as DAMA [31] and KIMS [32]), cryogenic semiconductor detectors (such as SuperCDMS/CDMS [33], EDELWEISS [34] and CRESST [35]), noble liquid detectors (such as ZEPLIN III [36], XENON100 [37], LUX [38], or WARP [39]), or superheated liquid detectors (such as PICASSO [40] and COUPP [41]).

1.3.2 Indirect Detection

Indirect dark matter detection aims to see the by-products of DM either annihilating with itself or decaying into some detectable SM particle. It is typically expected that the by-products would be gamma rays, neutrinos, or SM particle/antiparticle pairs. To do indirect searches for DM, experiments look in regions where DM is thought to be the most dense, for example near stars or black holes. More annihilation events could be taking place in these regions, so the experiments look for excess amounts of the resulting SM particles.

1.3.3 Production

The production of dark matter could be possible in high-energy colliders such as the Large Hadron Collider (LHC) at CERN or the Belle II lepton collider at SuperKEKB which collide SM particles and produce many by-products (and subsequent decays), one of which could be dark matter. The experiments look for missing mass and momentum in the collision by-products. These experiments have searched for missing mass in decays and have been able to put several constraints on the characteristics of DM.

1.4 SuperCDMS

The SuperCDMS experiment is a leading direct detection DM experiment that uses cryogenic semiconductor detectors to search for dark matter. The sub-Kelvin cooled detectors can achieve very low energy thresholds, which make the experiment sensitive to both typically WIMP regimes, as well as lighter dark matter candidates (namely, LDM and ALPs).

1.4.1 SNOLAB

The SuperCDMS experiment is currently being set up, 2 kilometers underground at SNOLAB in Sudbury, Ontario Canada. The previous data run of the experiment took place underground in a mine in Soudan, Minnesota. The SNOLAB is a significantly deeper and cleaner lab environment compared to the Soudan mine. This makes the installation and run have much more background shielding, which will lead to smaller detection sensitivities. The SNOLAB operation will use several towers which consist and stacks of roughly hockey-puck-sized detectors. The run is expected to go for roughly 5 years with 80 % live time. SuperCDMS at SNOLAB is expected to achieve leading sensitivities for generic WIMP-nucleon scattering in the low GeV mass range. The CUTE (Cryogenic Underground TEst) facility at SNOLAB is already in operation with a few of these detector towers, and the SuperCDMS experiment is expected to begin within the next year.

1.4.2 Detector Mechanisms

SuperCDMS uses a dilution refrigerator that cools the detectors to roughly 15 mK via a cold stem which conducts heat. The detector towers are shielded behind multiple layers of neutron and gamma-ray shielding. An electronic stem carries out signals from the detectors to the electronics tank which is in a vacuum tank where the detector readout boards (DCRCs) are connected. The entire SuperCDMS experiment is placed on a seismic platform to reduce seismic events affecting the experiment. The experimental schematic is shown in Figure 1.6.

The SuperCDMS semiconductor detectors are made with either Germanium or Silicon. Particle interactions within the detector, correspond to either electron or nucleus recoils. The

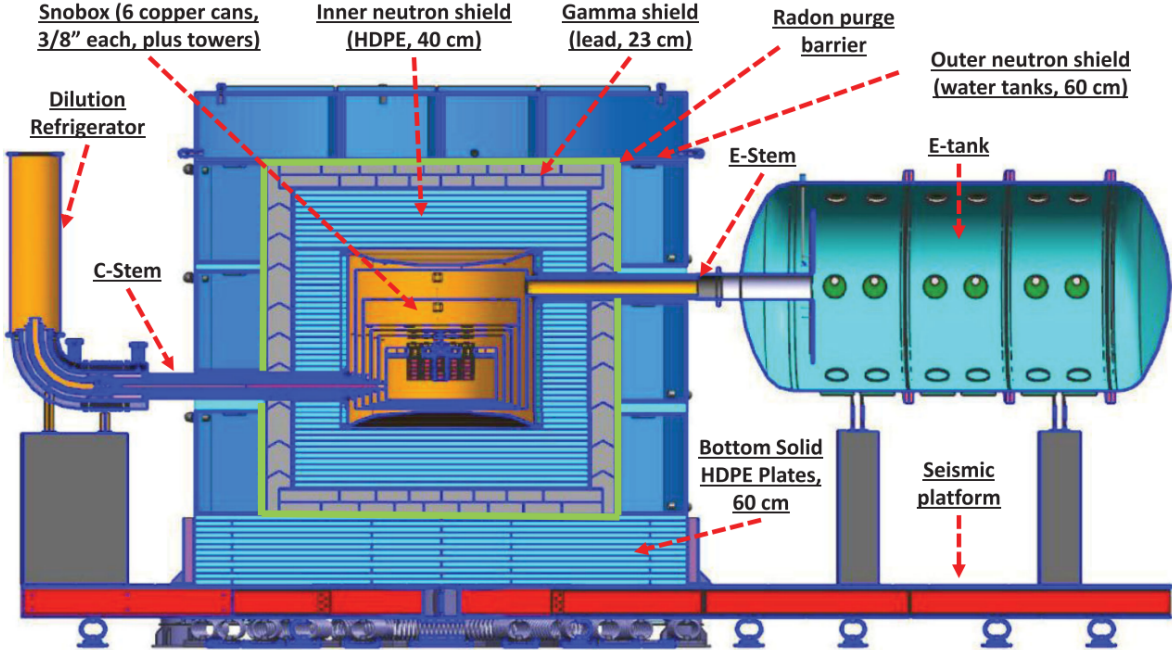


Figure 1.6: The SuperCDMS experimental schematic. Taken from the SuperCDMS collaboration paper [6].

recoil produces electron-hole pairs and some initial recoil lattice vibrations (phonons). The charged carrier (electron and hole) are pulled across the detector via an applied electric field. This drifting of charge carriers through a potential difference generates Neganov-Trofimov-Luke (NTL) phonons via the NTL effect which creates an amplified number of phonons that can be trapped by sensors on the outside of the detector and later digitized into a time series signal (see Figure 1.7).

The phonons are measured with quasi-particle trap electrothermal feedback transition edge sensors (QETs). The phonons travel to the outside of the detector where the QETs have superconducting aluminum collector fins which absorb phonons in the breaking of Cooper pairs. The resulting broken Cooper pairs are quasi-particles which enter into a Tungsten transition edge sensor (TES). The tungsten is in transition between superconducting and normal conducting, so the quasi-particles that enter the tungsten heat up the temperature of the TES on short timescales which leads to a rapid increase in the TES resistance (see Figure 1.8).

This analog resistance signal is amplified in a superconducting quantum interference device (SQUID) circuit and digitized with the SuperCDMS readout boards (DCRC). SuperCDMS has two main detector designs called the interleaved Z-sensitive ionization and phonon (iZIP) detector, and the high voltage (HV) detector. The iZIP detector has the additional benefit of being able to measure charge via interleaved electrodes on the detector, which allows for discrimination between electron and nucleus recoil events (leading to less background in energy spectrum analysis). The HV detectors have the added benefit of running at much higher voltages and thus create a large amount of NTL phonons and have lower energy thresholds. The SuperCDMS experiment uses a combination of these detectors in unison to get the best possible results. More specifically the SuperCDMS is projected to get world-leading results in the sub to low GeV mass range of dark matter candidates (see Figure 1.9).

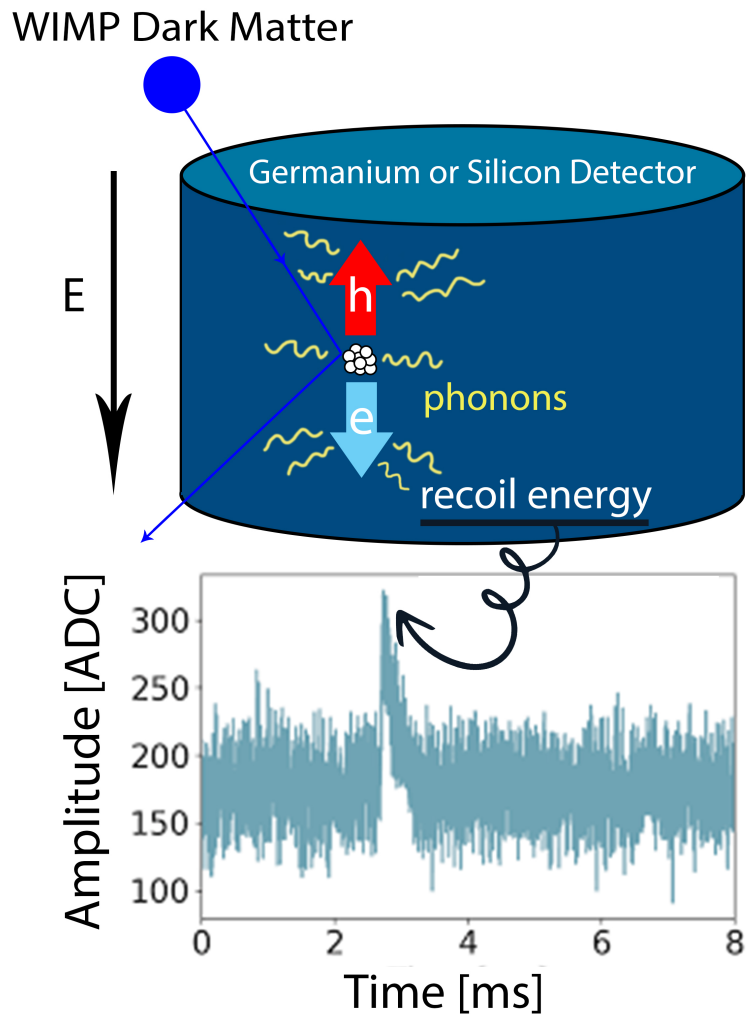


Figure 1.7: Schematic representation of energy recoil in a SuperCDMS detector (upper). The recoil creates lattice vibrations (phonons) that get captured by sensors on the face of the detector. An example trace of the digitized energy is shown (lower). Adapted from [7].

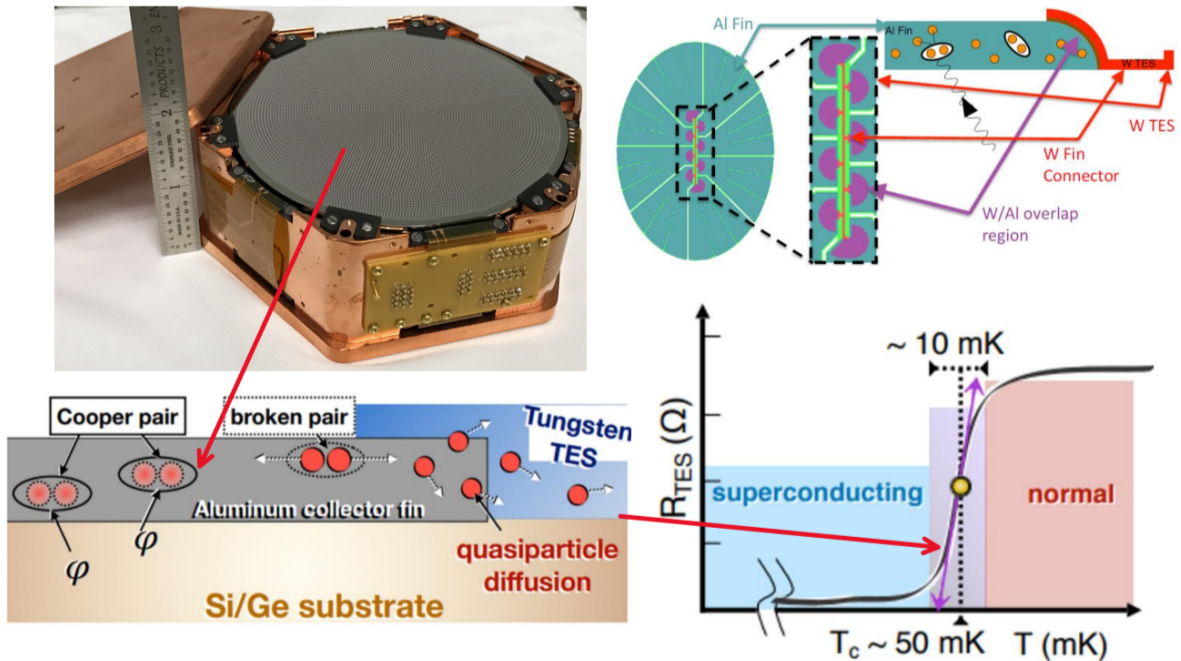


Figure 1.8: QET detector mechanism schematic. Figure put together with sub-figures from the SuperCDMS collaboration.

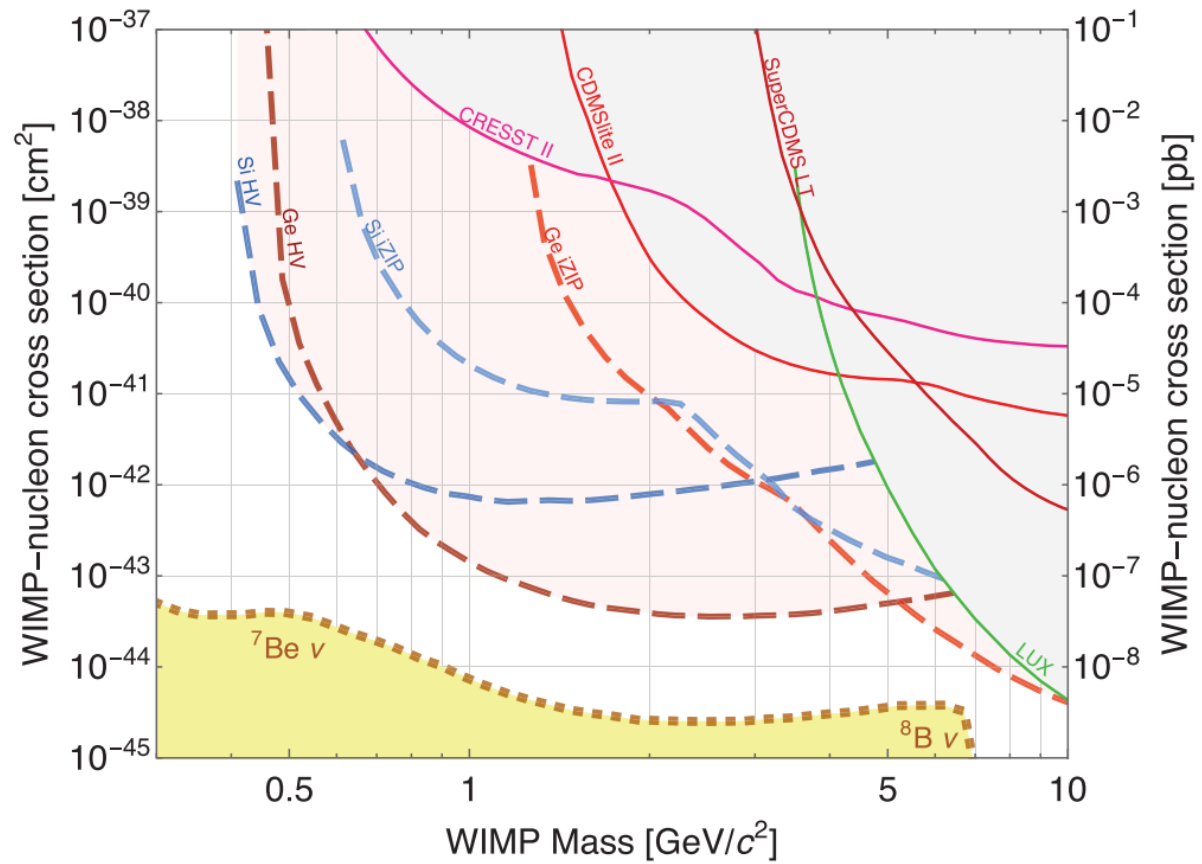


Figure 1.9: The projected dark matter sensitivities for the SuperCDMS SNOLAB run. Taken from the SuperCDMS collaboration paper [6].

Chapter 2

Energy Reconstruction

Accurate energy estimation is key to distinguishing dark matter events from backgrounds. SuperCDMS detectors are precisely calibrated so that the amplitude of the digitized events can be converted to the amount of energy that was deposited in the detector events. Noise in the time-series data necessitates a thoughtful approach to amplitude estimation, especially when the time-domain signal is buried in the noise. SuperCDMS uses optimal filter (OF) techniques, which harness the known signal template and noise template to make amplitude estimates in the frequency domain. The OF allows for accurate estimation of deposited energy in detector events.

A long run collects many time-series events. The events originate from an assortment of particles and an energy spectrum is created where different known backgrounds account for sections of the distribution. The theorized WIMP DM would generate an exponential distribution signature left over in the distribution after each background is accounted for (see Figure 2.1).

The conventional approach assumes uncorrelated frequencies in noise, a simplification that slightly diverges from reality but significantly simplifies computation. Ultimately, the success of distinguishing whether an observed signal is indicative of dark matter or another phenomenon crucially relies on our ability to precisely resolve the energy deposited in detectors. In the following sections, the traditional OF and computational underpinnings of this method will be discussed.

2.1 Traditional Optimal Filter

The essential foundation of OFs for event reconstruction in SuperCDMS has been laid out in more depth in Appendices A and B from Filippini’s 2008 thesis [42] as well as Appendix E from Thakhur’s 2015 thesis [8]. In the following section, I will closely follow some of their approach.

The OF becomes extremely useful when one needs to extract a signal $S(t)$, of known shape $A(t)$, from a background of known random noise $n(t)$ that is stationary and Gaussian. Stationary noise is defined to be noise that maintains consistent statistical properties over time, meaning for example that the noise variance and mean remain the same.

$$S(t) = aA(t) + n(t) \tag{2.1}$$

This is illustrated by an example case [8] in figure 2.2. The SuperCDMS events denote instances of energy deposition in a detector, which result in the digitized pulses carrying information about events. Determining the amplitude estimate “ a ” from a given signal trace using known signal and noise templates is at the heart of OF event reconstruction.

One might initially consider a simple amplitude estimator based on peak values from a trace, but this method performs extremely poorly as the signal-to-noise ratio worsens. Moreover, it neglects the rich information in the shape of the signal.

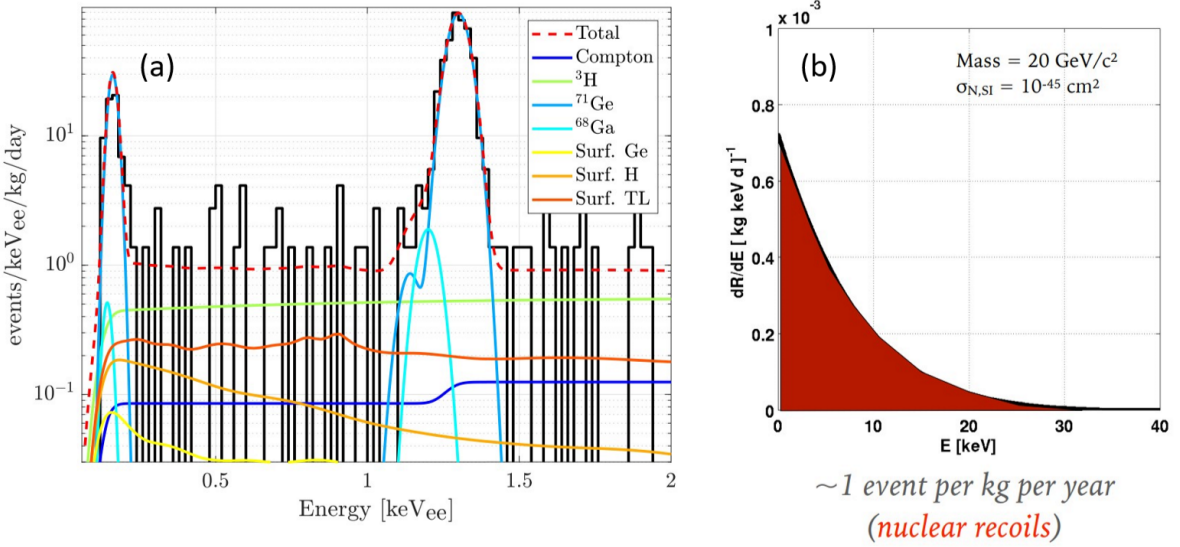


Figure 2.1: An example energy spectrum (a) after a run, with each part of the energy spectrum accounted for by various known background signal distributions (taken from [6]). An example of the theoretical exponential dark matter energy distribution (b) signature based on the cross-section and mass of the dark matter (taken from SuperCDMS collaboration member, Jodi Cooley at SMU).

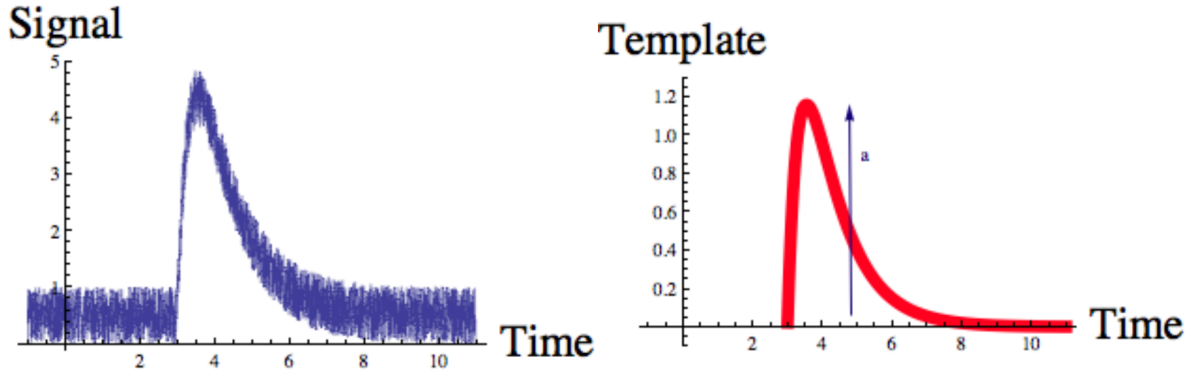


Figure 2.2: Example case from SuperCDMS (Ref [8]) with the left plot showing the signal ($S(t) = a \cdot A(t) + n(t)$) and the right plot showing the fit ($a \cdot A(t)$)

An alternative approach involves employing a time-domain χ^2 and minimizing it to fit for the amplitude estimator. This would take the form of

$$\chi_{TD}^2(a) = \sum_k \frac{(S_k - aA_k)^2}{\langle n_k^2 \rangle} \quad (2.2)$$

However, this method assumes statistical independence of noise fluctuations in consecutive time bins, corresponding to white noise, which is not the case in scenarios with non-trivial noise.

Transitioning to the frequency domain, the assumption that the noise is stationary and Gaussian implies that each frequency bin is uncorrelated with others. This enables the computation of a frequency domain χ^2 , and the corresponding minimization used to solve for the amplitude estimator. Additionally incorporating a complex exponential component to account for the pulse's shift within the trace, the frequency domain χ^2 takes the form of:

$$\chi_{FD}^2(a, t_0) = \sum_n \frac{|\tilde{S}_n - ae^{-2\pi i t_0 f_n} \tilde{A}_n|^2}{V_n} \quad (2.3)$$

where \tilde{S}_k and \tilde{A}_k are Fourier-transformed components, and V_n accounts for noise (co)variance in the frequency domain (from the power spectral density of a sample of noise traces).

2.2 Computational Underpinnings

To simplify notation for further discussion on the computational underpinnings of the OF, we can let \tilde{S}_k just be the data and $ae^{-2\pi i t_0 f_n} \tilde{A}_n$ be the expected value.

The full form of the χ^2 in the case where all the frequencies are correlated with each other would take the form of

$$\chi^2 = \sum_i \sum_j (\text{Data} - \text{Expected})_i (\text{Data} - \text{Expected})_j (V^{-1})_{ij}, \quad (2.4)$$

where

$$V_{ij} = \langle \tilde{n}^2 \rangle_{ij} = \begin{bmatrix} \sigma_1^2 & \dots & \rho_{(N,1)} \sigma_N \sigma_1 \\ \vdots & \ddots & \vdots \\ \rho_{(1,N)} \sigma_1 \sigma_N & \dots & \sigma_N^2 \end{bmatrix}$$

It turns out that the standard matrix inversion algorithm time complexity of $O(n^3)$. This means that with a large number (thousands) of frequencies, the computation for inverting V is impractical. Additionally, the inversion problem is extremely ill-conditioned for large matrices. Ill-conditioned problems mean that any small numerical rounding errors in the input lead to large changes in the output.

If frequencies are assumed to be uncorrelated, V is diagonal, and we get a convenient covariance matrix of

$$V_{ij} = \begin{bmatrix} \sigma_1^2 & & & \\ & \sigma_2^2 & & 0 \\ & & \sigma_3^2 & \\ 0 & & & \ddots \\ & & & & \sigma_n^2 \end{bmatrix} \quad (2.5)$$

or simplified as

$$V_{ij} = \delta_{ij}\sigma_i^2 \quad (2.6)$$

The corresponding χ^2 avoids any complicated matrix inversion, since here we only need to invert each of the covariances along the diagonal one by one:

$$\chi^2 = \sum_i \frac{(\text{Data} - \text{Expected})_i^2}{V_i} \quad (2.7)$$

Next, we should consider that the noise at any frequency can be expressed as a sum of sin and cos functions where each additional term has a random Gaussian amplitude (centred at 0 and where a larger Gaussian spread indicates that the noise is stronger).

$$n(t) = \sum_{\omega} A_{\omega} \sin \omega t + B_{\omega} \cos \omega t \quad (2.8)$$

If we take the Fourier transform of the noise we then get $|J(f)| = |A_f + iB_f|$, where J is the Fourier transform of the noise. This gives a power spectral density (PSD) of the form

$$|J(f)|^2 = A_f^2 + B_f^2 + 2 \operatorname{Cov}(A_f B_f) \quad (2.9)$$

where A and B are a list of the real and imaginary components of the PSD at different frequencies.

Using the fact here that each frequency of the noise has a real and imaginary component we can more precisely write a purely real covariance matrix as

$$V = \begin{bmatrix} \begin{bmatrix} \langle A^2 \rangle & \langle AB \rangle \\ \langle AB \rangle & \langle B^2 \rangle \end{bmatrix}_{f_1} & 0 \\ & \ddots \\ 0 & \begin{bmatrix} \langle A^2 \rangle & \langle AB \rangle \\ \langle AB \rangle & \langle B^2 \rangle \end{bmatrix}_{f_n} \end{bmatrix} \quad (2.10)$$

Here the diagonal matrices show the variance and covariance of the real and imaginary parts at the frequency f_n of the PSD. This comes from the average at a particular frequency f_n computed from several noise traces. The χ^2 is then

$$\begin{aligned} \chi^2 = \sum_f & \left((\text{Data}_{\text{Re}} - \text{Expected}_{\text{Re}}), (\text{Data}_{\text{Im}} - \text{Expected}_{\text{Im}}) \right)_f \\ & \begin{bmatrix} A^2 & AB \\ AB & B^2 \end{bmatrix}_f^{-1} \left((\text{Data}_{\text{Re}} - \text{Expected}_{\text{Re}}), (\text{Data}_{\text{Im}} - \text{Expected}_{\text{Im}}) \right)_f \end{aligned} \quad (2.11)$$

We then assume that the variance terms are nonzero and the covariance terms are 0 (i.e. that the real and imaginary parts are uncorrelated). This simplifies the case back to the simple computation that we previously found in equation (7) with only the additional fact that for every frequency we get 2 terms instead of 1 (corresponding to the real variance and the imaginary variance).

$$|J(f)|^2 = A_f^2 + B_f^2 \quad (2.12)$$

$$V = \begin{bmatrix} \left[\begin{array}{cc} \langle A^2 \rangle & 0 \\ 0 & \langle B^2 \rangle \end{array} \right]_{f_1} & & 0 \\ & \ddots & \\ 0 & & \left[\begin{array}{cc} \langle A^2 \rangle & 0 \\ 0 & \langle B^2 \rangle \end{array} \right]_{f_n} \end{bmatrix} \quad (2.13)$$

and again a corresponding χ^2 of

$$\chi^2 = \sum_f \left((\text{Data}_{\text{Re}} - \text{Expected}_{\text{Re}}) \quad (\text{Data}_{\text{Im}} - \text{Expected}_{\text{Im}}) \right)_f \cdot \left[\begin{array}{cc} \langle A^2 \rangle & 0 \\ 0 & \langle B^2 \rangle \end{array} \right]_f^{-1} \left((\text{Data}_{\text{Re}} - \text{Expected}_{\text{Re}}) \quad (\text{Data}_{\text{Im}} - \text{Expected}_{\text{Im}}) \right)_f. \quad (2.14)$$

Computing this simplified form of χ^2 is computationally realistic and performs well. Under the assumptions laid out, minimizing the χ^2 function by taking its derivative yields the best possible fit results for the amplitude a and time delay t_0 . The simplified expression for the χ^2 if we assume centered pulses is;

$$\chi^2(a) = \sum_f \frac{|\tilde{S}_f - a\tilde{A}_f|^2}{\langle \tilde{n}^2 \rangle_f} \quad (2.15)$$

with an amplitude estimate solution of,

$$\hat{a} = \frac{\sum_f \frac{\tilde{A}_f^* \tilde{S}_f}{\langle \tilde{n}^2 \rangle_f}}{\sum_f \frac{|\tilde{A}_f|^2}{\langle \tilde{n}^2 \rangle_f}} \quad (2.16)$$

Thus, with a time-series event, a noise template and a pulse template, the amplitude of the noisy pulse can be quickly computed even if the noise buries the pulse in the time domain. This method has been the ‘optimal’ method for event reconstruction of the energy deposited by extremely small particle interactions in the SuperCDMS detector events.

Chapter 3

Correlation Clustering Optimal Filter

The question then arises: what happens when dealing with correlated frequencies in noise? This question is at the heart of this thesis.

3.1 Non-Stationary Noise

In an ideal setting, the standard OF in SuperCDMS assumes that the different noise frequencies (bins) are uncorrelated. This corresponds to stationary noise. However, real-world conditions such as dilution fridge pulse tube noise or odd harmonics of noise from electrical sources could introduce a dynamic environment characterized by numerous correlated frequencies within the noise profile, leading to non-stationary noise.

3.1.1 Non-diagonal Correlation Matrix Example

An example of a partial correlation matrix is shown in Figure 3.1. The correlation matrix is the normalized version of the covariance matrix that is dimensionless and allows for proper visualization of the scale of correlation at different frequencies. This correlation matrix is calculated from noise data from the SuperCDMS experiment and clearly shows off-diagonal correlations (non-blue colour). The real noise diverges from stationary noise expectation that frequencies are uncorrelated (which would correspond to a simple diagonal correlation matrix). These correlated frequencies are a computational challenge to address. To fully account for the correlations in the noise, it would require a full version of the χ^2 calculation,

$$\chi^2(a) = \sum_i \sum_j (\tilde{S}_i - a\tilde{A}_i) \langle \tilde{n}^2 \rangle^{-1}_{ij} (\tilde{S}_j - a\tilde{A}_j)^*, \quad (3.1)$$

and a corresponding amplitude estimate equation,

$$\hat{a} = \frac{\sum_i \sum_j \tilde{A}_i^* \langle \tilde{n}^2 \rangle^{-1}_{ij} \tilde{S}_j}{\sum_i \sum_j \tilde{A}_i^* \langle \tilde{n}^2 \rangle^{-1}_{ij} \tilde{A}_j}. \quad (3.2)$$

3.1.2 Matrix Inversion Complexity and Condition Number

When dealing with matrix inversion in programming environments like Python with libraries such as NumPy and SciPy, the Gauss-Jordan elimination algorithm is commonly employed, characterized by a complexity of $O(n^3)$. This indicates that the computational effort increases rapidly with the cube of the size of the matrix. In this thesis, the analysis focuses on down-sampled traces comprising only 100 bins initially, facilitating a simplified comparison of the various OF methods.

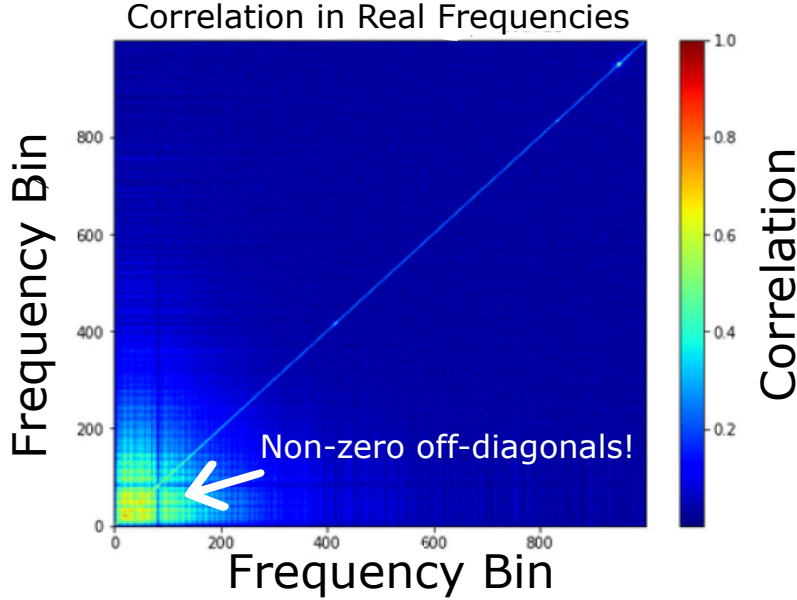


Figure 3.1: An example of a simple colour map plot showing the correlation matrix for the real component of 1000 of the noise frequency bins. Noise taken from SuperCDMS.

Moving to numerical analysis, the condition number of a function serves as a measure of how sensitive the function's output is to small changes in its input. It gauges the extent to which alterations or inaccuracies in the input lead to errors in the output. This concept originates from the theory of uncertainty propagation, quantifying the worst-case relative change in output for a given relative change in input.

A low condition number suggests that a problem is well-conditioned, indicating that minor changes in the input lead to only negligible variations in the output. Conversely, a high condition number indicates an ill-conditioned problem, where even slight alterations in the inputs result in substantial changes in the output, making it difficult to accurately determine the solution. In the context of this thesis, Python packages can be utilized to compute the condition number of the inversion problem. For the 100-bin matrices analyzed in this study, the resulting condition number is several thousand, significantly deviating from the ideal value of 1, indicating an ill-conditioned problem with significant errors in the inversion output.

Considering that full SuperCDMS traces consist of over 30,000 bins, dealing with their computational complexity, coupled with the even more ill-conditioned inversion problem, presents considerable challenges in accurately estimating the amplitude of an event using the full OF method.

3.2 Cluster Sort Method

3.2.1 Novel Optimal Filter Application

This challenge necessitates a novel approach to simplify the expensive and error-prone computation of χ^2 for correlated frequencies:

$$\chi^2 = \sum_i \sum_j (\text{Data} - \text{Expected})_i (\text{Data} - \text{Expected})_j (V^{-1})_{ij} \quad (3.3)$$

3.2. Cluster Sort Method

The correlation matrix can be used to identify the highly correlated frequency clusters within the full covariance matrix. More specifically, since an inversion of the full covariance matrix,

$$V = \begin{bmatrix} \begin{bmatrix} \langle A^2 \rangle & \langle AB \rangle \\ \langle AB \rangle & \langle B^2 \rangle \end{bmatrix}_{f_1} & \cdots & \begin{bmatrix} \langle A_{f_n} A_{f_1} \rangle & \langle A_{f_n} B_{f_1} \rangle \\ \langle B_{f_n} A_{f_1} \rangle & \langle B_{f_n} B_{f_1} \rangle \end{bmatrix} \\ \vdots & \ddots & \vdots \\ \begin{bmatrix} \langle A_{f_1} A_{f_n} \rangle & \langle A_{f_1} B_{f_n} \rangle \\ \langle B_{f_1} A_{f_n} \rangle & \langle B_{f_1} B_{f_n} \rangle \end{bmatrix} & \cdots & \begin{bmatrix} \langle A^2 \rangle & \langle AB \rangle \\ \langle AB \rangle & \langle B^2 \rangle \end{bmatrix}_{f_n} \end{bmatrix}, \quad (3.4)$$

cannot realistically be computed, a correlation clustering algorithm can be used to cluster the frequencies based on their correlations (clusters shown as matrices X , Y , Z below). With the clusters along the diagonal, and the off-diagonal terms set to zero. The matrix will then be block diagonal,

$$\begin{bmatrix} [X] & & 0 \\ & [Y] & \\ 0 & & [Z] \end{bmatrix}, \quad (3.5)$$

and each cluster can be individually inverted,

$$\begin{bmatrix} [X]^{-1} & & 0 \\ & [Y]^{-1} & \\ 0 & & [Z]^{-1} \end{bmatrix}. \quad (3.6)$$

A simplified schematic showing the general procedures of the three OF methods (diagonal, cluster sort, and full) is shown in Figure 3.2. The currently used diagonal method ignores any potential large correlations in the noise (signified by blue squares) on the far left matrix. The diagonal method inverts each value along the covariance matrix diagonal and sets all the off-diagonal terms to zero. Note that the simplified schematic does not show the covariance matrix in the steps. The full method takes the full covariance matrix (related to the correlation matrix shown in the schematic) and inverts the entire thing. Although the schematic shows a matrix with 10 bins, the larger scale version of this inversion would introduce the errors and time complexity previously discussed. Additionally, there is some statistical error that is introduced from the fact that the covariance matrices are built with a finite number of noise traces. This means that if, in theory, a frequency covariance bin would average out to zero, the finite nature of the data will lead to small non-zero terms that can propagate errors into the full inverse method. This means that setting certain bins to zero could potentially lead to better results than the full method.

The cluster sort method is the main focus of this thesis. The clustering algorithm (discussed more in subsequent sections) groups the correlated frequency bins in a block diagonal. The inverse of each of the clusters is computed and then the values of each bin can easily be remapped to their original indices, which gives an approximate inverse covariance matrix. This methodology maintains the largest covariance off-diagonal terms, as demonstrated in Figure 3.2. This method better accounts for large off-diagonals in the covariance matrix compared to the over-simplified off-diagonal terms in the traditional diagonal OF that SuperCDMS currently uses. This method additionally remains computationally reasonable since the inversions it needs to perform are much smaller than the size of the full covariance matrix.

3.2.2 Correlation Clustering

Correlation clustering is a generic class of algorithms which offer a method for organizing a set of objects into clusters based on their inherent relationships, without the need to predetermine

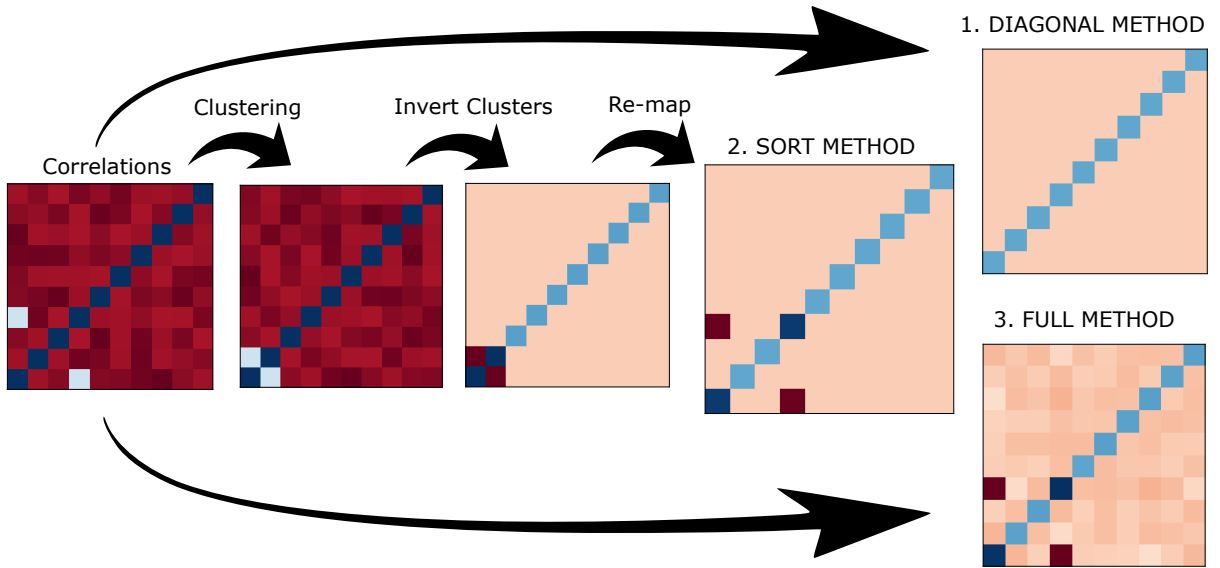


Figure 3.2: A simplified schematic of the three OF methods, focusing on the construction of the inverse covariance matrix (simplified to the inverse correlation matrix in this diagram). The cluster sort method is shown to preserve the large off-diagonal terms that the diagonal method ignores.

the number of clusters. Unlike traditional clustering approaches, correlation clustering operates under the premise that the correlation between bins is known. In this paradigm, the correlation matrix is equivalent to a weighted graph that has edge weights close to 1 to denote correlation and edge weights close to 0 to signify dissimilarity. The objective of this kind of algorithm is to identify a clustering that maximizes agreements (correlation) or minimizes disagreements (low-correlations) among the bins. It is noted that perfect clustering is not always attainable. Various algorithms, developed largely for machine learning, offer approximation solutions to this problem. One such algorithm is the CC-Pivot algorithm by Ailon et. al. [43], which is used as the basis for the implementation of the correlation clustering algorithm for the optimal filter, done in this thesis. The commented Python function 3.1 is provided to illustrate the steps in the clustering algorithm.

The function takes as an input, either the real or imaginary correlation matrix, and an input threshold value to determine the level of correlation desired for clustering. It iteratively selects a random pivot node and forms a cluster around it by adding nodes that surpass the specified correlation threshold. The process continues until all nodes are assigned to clusters. This approach effectively groups highly correlated frequencies into clusters.

A schematic example is shown in Figure 3.3, where 2 main clusters larger than size one are identified and resorted along the diagonal. Note the figure indicates the bin indices and the resulting clustering which rearranges the matrix indices. Both the x-axis and the y-axis have the same frequency index values.

3.3 Covariance Sorting with Cluster Mapping and Remapping

The clusters are made with a real or imaginary correlation matrix that is half the size of the full covariance matrix, which contains both real and imaginary components of the covariance for each frequency. For both of these matrices, it is noted that the DC frequency bins are removed

Program 3.1 Commented Python function that clusters highly correlated frequencies.

```

def CC_Pivot(correlation_matrix, thresh=0.6):
    """
        Clustering using Pivot Algorithm (developed by Ailon et. al.)
    Args:
        - correlation_matrix (2D numpy array): Matrix representing pairwise
            correlations between nodes.
        - thresh (float, optional): Threshold value for correlation. Default is 0.6.
    Returns:
        - clusters (list of sets): List of clusters where each cluster is
            represented as a set of nodes.
    """
    # Get the number of nodes in the correlation matrix
    num_nodes = len(correlation_matrix)
    # Initialize an empty list to store clusters
    clusters = []
    # Create a set containing all node indices
    V_prime = set(range(num_nodes))

    # Iterate until all nodes are assigned to clusters
    while V_prime:
        # Randomly choose a pivot node from the remaining nodes
        pivot = np.random.choice(list(V_prime))
        # Initialize a new cluster with the pivot node
        cluster_C = {pivot}
        # Initialize a new set to store nodes that do not meet the threshold
        V_prime_new = set()

        # Iterate through all nodes in V_prime
        for j in V_prime:
            # Check if the correlation between the pivot node and node j is
            # above the threshold
            if correlation_matrix[pivot, j] > thresh:
                # Add node j to the cluster if the correlation is
                # above the threshold
                cluster_C.add(j)
            else:
                # Otherwise, add node j to the new set of nodes that do not
                # meet the threshold
                V_prime_new.add(j)

        # Add the current cluster to the list of clusters
        clusters.append(cluster_C)
        # Update V_prime to contain only the nodes that do not belong to
        # any cluster yet
        V_prime = V_prime_new
    # Return the list of clusters
    return clusters

```

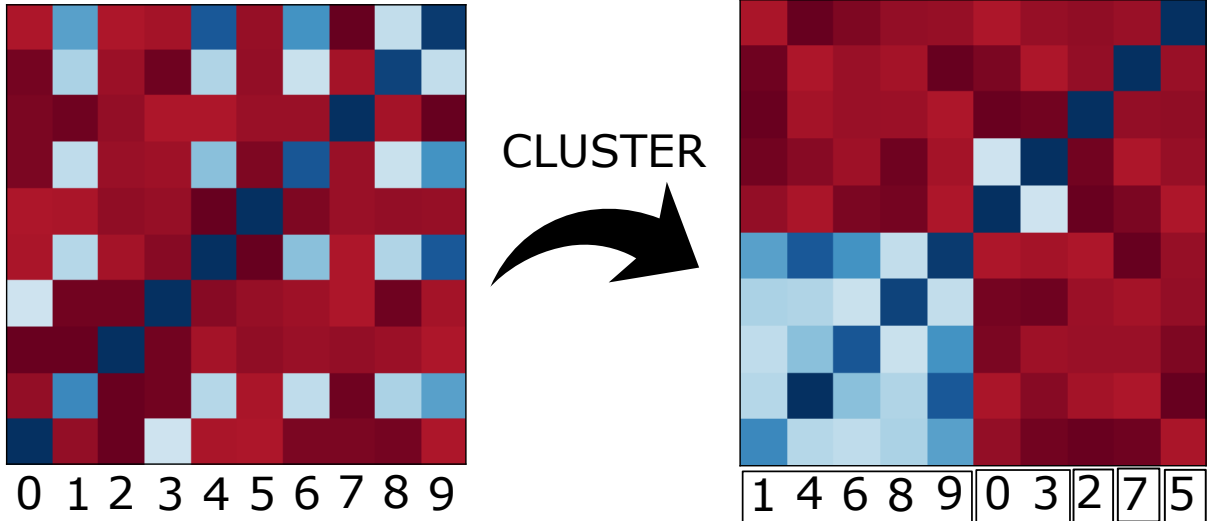


Figure 3.3: A simple clustering example with a 10x10 matrix. Dark blue values represent large correlations and dark red values represent no correlation. The index clusters are used to rearrange the indices to be block diagonal in the right subplot.

as well as the negative frequency bins which contain no new information since the time series noise is all real values. The clusters then need to get mapped to the full covariance indices. The real and imaginary parts are assumed to stay together in the same clusters. Thus for each index in a cluster, the mapping adds two indices to the covariance cluster. For example, index 0 is mapped to indices 0 and 1, and index 1 is mapped to indices 2 and 3, and so on until all indices in the covariance matrix are accounted for. The block diagonal is then assembled with the covariance matrix and the corresponding covariance clusters. The inverse of each other block-diagonals is computed and all other off-diagonals are set manually to zero. Then a remapping is done to return the bins to their original indices. This method successfully preserves the large off-diagonal correlation matrix information.

Chapter 4

Results and Discussion

4.1 Analysis Approach

The three methods are compared with the amplitude estimate derived from the χ^2 minimization. Namely, for the cluster sort method and full method this is;

$$\hat{a} = \frac{\sum_i \sum_j \tilde{A}_i^* \langle \tilde{n}^2 \rangle^{-1}_{ij} \tilde{S}_j}{\sum_i \sum_j \tilde{A}_i^* \langle \tilde{n}^2 \rangle^{-1}_{ij} \tilde{A}_j}, \quad (4.1)$$

and for the diagonal method, this simplifies to;

$$\hat{a} = \frac{\sum_f \frac{\tilde{A}_f^* \tilde{S}_f}{\langle \tilde{n}^2 \rangle_f}}{\sum_f \frac{|\tilde{A}_f|^2}{\langle \tilde{n}^2 \rangle_f}}. \quad (4.2)$$

The cluster sort method uses a correlation threshold of 0.3 unless otherwise noted. For the first analysis, 1000 non-stationary noise time series were simulated. Then for the second analysis, 1000 real noise data from the SuperCDMS lab is used and down-sampled to make the analysis more efficient. The simulated and real noise data was used to compute the inverse covariance matrix term in the amplitude estimate equations above for all three methods. Each noise time series is then added to a centered scaled template of a known shape. The template being centered in the time series means that this analysis and thesis work only addresses finding the amplitude estimate and has not yet addressed finding the time shift that is also needed for the real experiments analysis. The scaling on the template is what the OF methods aim to retrieve during analysis. A scale of 1 is always used unless otherwise noted. This value is arbitrary and the methods show similar results regardless of the scale used, as will be discussed in a subsequent subsection. Thus all three methods make a computation of the amplitude estimate of all 1000 noisy pulses. The resulting amplitude estimates are roughly Gaussian distributed around the pre-set amplitude scale. The analysis hinges on the fact that the standard deviation of the amplitude estimate distribution is proportional to the energy resolution of the method. This means that a smaller standard deviation in the distribution resulting from one of the methods, results in a better energy resolution from that method and leads to stronger confidence in the energy spectrum results for the SuperCDMS experiment.

4.2 Simulated Non-Stationary Noise

The simulated non-stationary noise is generated using a combination of several square waves as defined by a partial (typically $N < 100$) square wave Fourier series,

$$f(x) = \frac{4}{\pi} \sum_{n=1,3,5,\dots}^N \frac{1}{n} \sin\left(\frac{n\pi x}{L}\right), \quad (4.3)$$

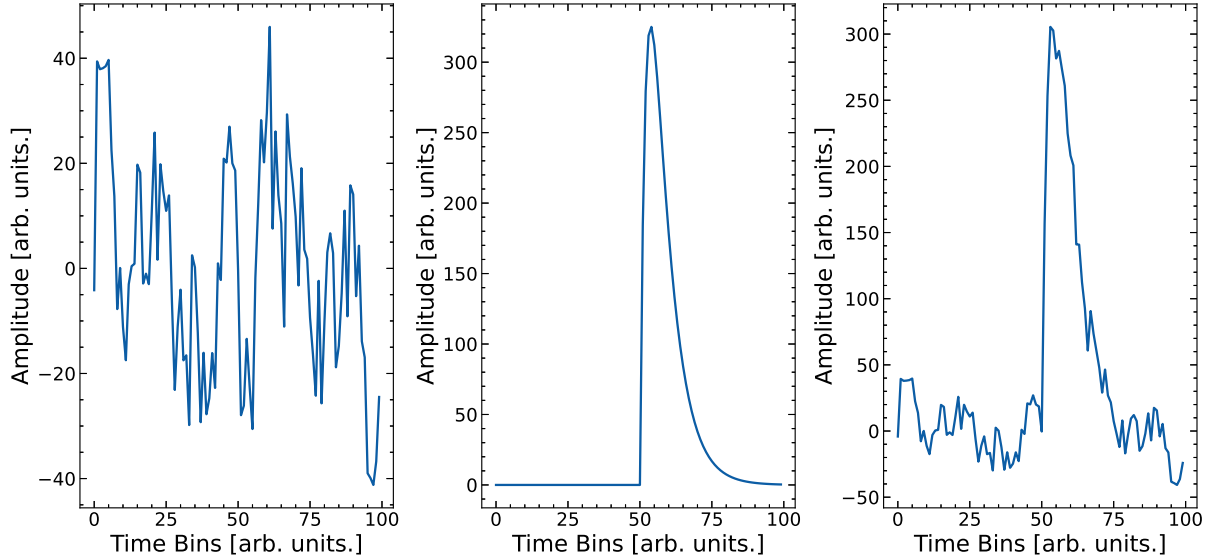


Figure 4.1: The left-most subplot shows an example of the simulated time series noise. The middle subplot is the scaled pulse template. The right-most subplot is the addition of the two other subplots.

with random white noise also added on top. An example of a simulated noise time series is illustrated in Figure 4.1, along with a scaled pulse template and the addition of the noise and pulse template.

The key feature of the simulated noise is that it is non-stationary and has forced large off-diagonal terms in the correlation/covariance matrices. The square wave terms are constructed using the first few terms of the Fourier series (rather than the infinite series) to mitigate over-correlation, which would lead to inconveniently large clusters. Moreover, deliberate avoidance of random shifts in the square wave phase further maximizes the off-diagonal elements. The idea with this simulated noise is that we are creating a noise condition where the diagonal method significantly diverges from being a good approximation.

This methodology yields a notable improvement of +10.28% and +0.35% over the diagonal and full methods, respectively, as depicted in Figure 4.2. These results align with the expectation that the diagonal method will perform poorly in non-stationary noise cases. The improvement over the full method is explained by the computational errors introduced with the full inversion of the large matrix as well as the statistical limitations of the close-to-zero off-diagonal terms which add error to the estimates.

4.3 Down-sampled Real Noise

The same analysis procedure is repeated on real noise from SuperCDMS that has been down-sampled to have the same number of bins (100) as the simulated case above. This keeps the analysis consistent and also keeps the computations relatively fast. An example of the noise trace and the added pulse are shown in Figure 4.3.

Here we find that there are small off-diagonals in real noise which leads to the results shown in Figure 4.4. A +22.35% and +0.31% improvement over full and diagonal methods respectively is achieved with the cluster sort method with these noise conditions.

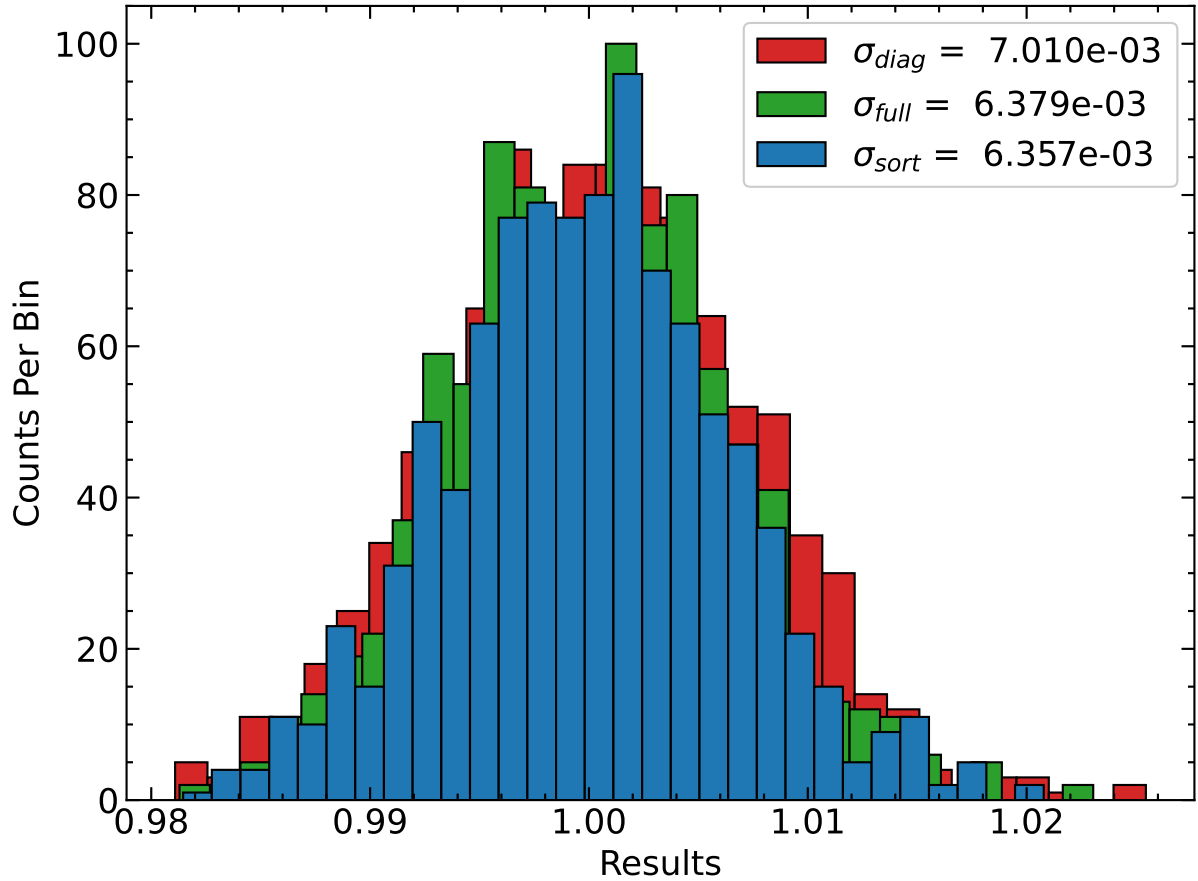


Figure 4.2: The simulated noise amplitude estimate results distribution is plotted in a histogram. The three methods are each applied on 1000 pulses. The standard deviation of each method is denoted in the legend.

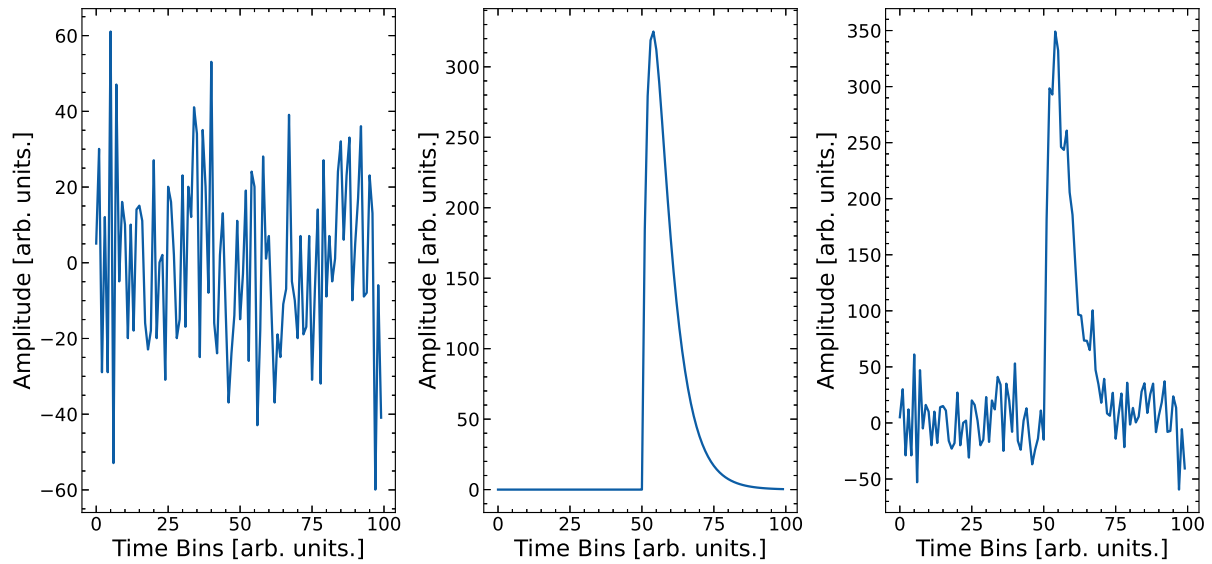


Figure 4.3: Real down-sampled time series noise and composite event example.

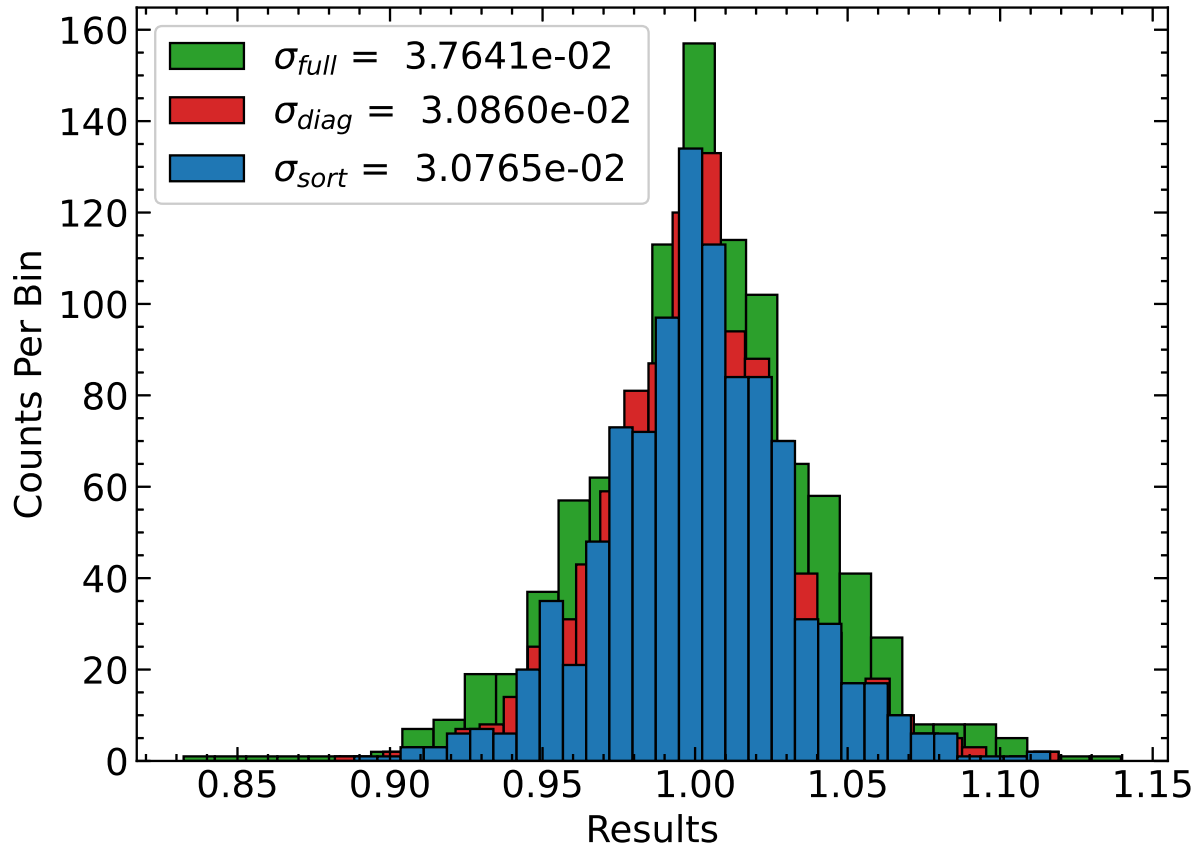


Figure 4.4: The real down-sampled noise amplitude estimate results distribution is plotted in a histogram. The three methods are each applied on 1000 pulses. The standard deviation of each method is denoted in the legend.

The results show that if there are only some small off-diagonal terms in the noise covariance matrix, the cluster sort method does not have a huge advantage over the diagonal approximation but the method protects itself from the errors introduced in the large matrix inversion of the full method.

4.4 Varying Analysis Parameters

In this section, the effects of varying parameters in the real noise analysis, on the performance of the methods are analyzed. We maintain consistent parameters throughout the experiments, including the number of bins per time series = 100, amplitude scale = 100, cluster correlation threshold = 0.3, and number of traces = 1000, except when that parameter is being varied.

The general observation from the experiments with real noise is that the full method exhibits suboptimal performance. This is attributed, as before, to the error introduced during the inversion of a large array using numerical methods and additionally, to the finite number of traces (1000) which introduces non-zero off-diagonal elements, which should ideally go to zero for white noise elements. Setting off-diagonal elements to zero, as done in the diagonal method, yields better results. Furthermore, both the diagonal and sorting methods perform similarly, with the sorting method showing slightly better performance.

When varying each parameter individually, it is observed that optimizing the clustering correlation threshold at 0.3 improves method performance (see Figure 4.5). Thresholds either too low or too high lead to suboptimal results, resembling the issues observed with the full method (large correlation threshold) or the diagonal method (small correlation threshold).

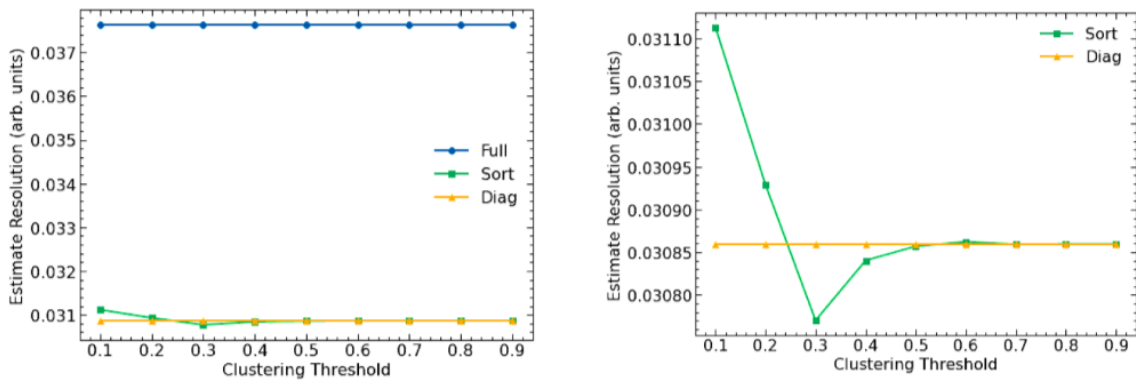


Figure 4.5: Effect of varying cluster correlation threshold on method performance. The optimal threshold for this noise is found to be 0.3.

Similarly, reducing the number of bins per trace to a minimum (50 in this case) significantly reduces inversion errors in the full method. However, increasing the number of bins provides more information about the frequencies in the noise, enhancing performance in the diagonal and sorting methods (see Figure 4.6).

Moreover, as suggested in an earlier section, the amplitude scale on the template does not significantly affect the overall results (see Figure 4.7). This indicates consistency of results for different deposited energies from a variety of particles.

Finally, increasing the number of traces seems to generally improve the performance of the full method, as it allows for better averaging out of white noise off-diagonal covariance terms.

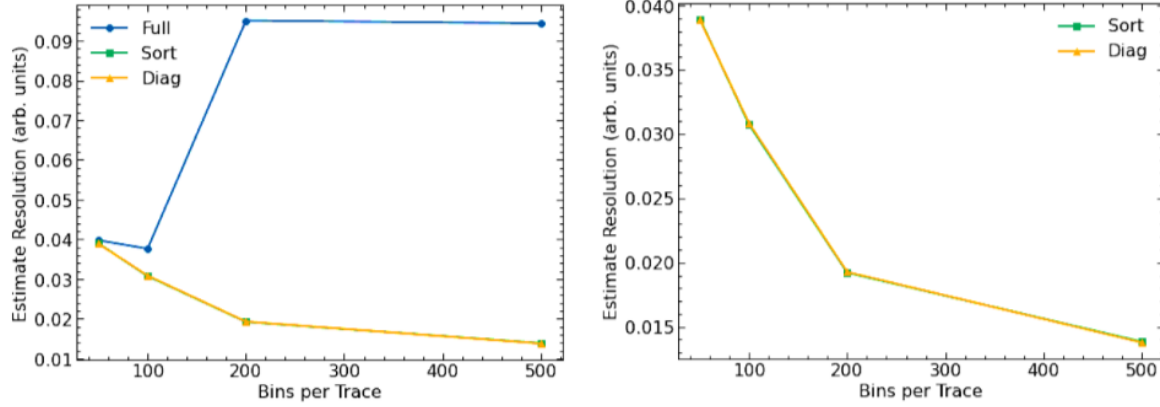


Figure 4.6: Effect of varying number of bins on method performance. Lowering the number of bins reduces inversion errors in the full method while providing more information about frequencies in the noise improves performance in the diagonal and sorting methods.

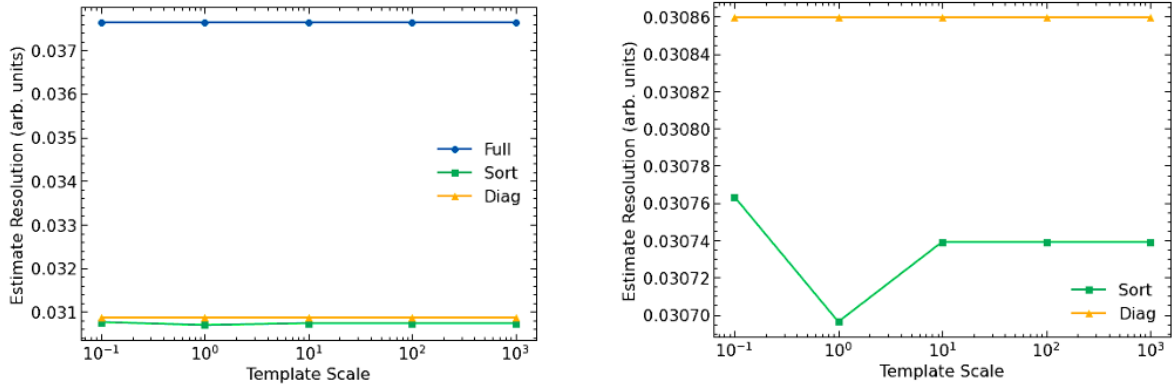


Figure 4.7: Effect of varying amplitude scale on template on method performance. The original results remain consistent regardless of whether the template dominates or is buried by the noise.

However, the sorting method is outperformed by the diagonal method when the number of traces is minimal. This is likely due to the statistical errors in the covariance matrix, which would produce large off-diagonals that would be incorrectly accounted for. An interesting observation is the uptick in performance of the full method with the largest number of traces (1560), which demonstrates the possible sensitivity to statistical scatter in measuring covariances. See Figure 4.8.

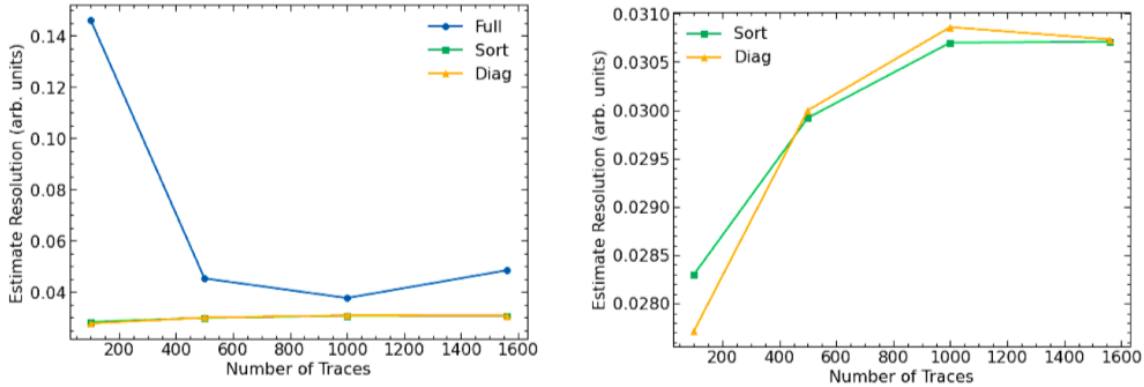


Figure 4.8: Effect of varying number of traces on method performance. Increasing the number of traces improves the performance of the full method, while the sorting method is outperformed by the diagonal method with a minimal number of traces.

4.5 Interpreting Results

The analysis of the results reveals distinct performance characteristics of the three methods under consideration. Firstly, the diagonal method exhibits suboptimal performance in scenarios where large off-diagonals are present in the covariance matrix, leading to inaccuracies in the amplitude estimation. Conversely, the full method, while theoretically comprehensive, proves inefficient and error-prone in practice. This inefficiency arises from both low statistics and ill-conditioned inversions, highlighting challenges in scalability and numerical stability. However, the cluster sort method emerges as a promising solution, effectively addressing the weaknesses of the other two methods. Notably, it demonstrates superior performance across varying types of noise, suggesting its robustness and adaptability in practical applications.

Chapter 5

Conclusion

5.1 Performance of Correlation Clustering

In conclusion, the novel correlation clustering OF method, developed in this thesis, is tested against other traditional OF methods. With SuperCDMS' potential for major breakthroughs in understanding new physics, the accurate resolution of energy deposited in the SuperCDMS detectors is crucial. Neglecting correlated frequencies within noise sources can lead to significant errors in the currently used OF method. However, the clustering methodology presented in this thesis proves to be a promising avenue for improvement by systematically accounting for correlations. By doing so, it not only safeguards against worst-case scenarios but also maintains computational feasibility, thus presenting a practical solution for enhancing the reliability and accuracy of experimental results.

5.2 Future Work

This work demonstrates a proof of method for the two cases addressed in the results section. Future work can take this method and apply it to full-size traces and then real events. Adding the capability to solve for the time shift in the template is an additional step that will need to be made for this method to scale up and be useable in the full SuperCDMS experiment.

Bibliography

- [1] E. Corbelli and P. Salucci. The extended rotation curve and the dark matter halo of m33. *Monthly Notices of the Royal Astronomical Society*, 311(2):441–447, jan 2000.
- [2] NASA/CXC/CfA/M.Markevitch et al.; Optical: NASA/STScI; Magellan/U.Arizona/D.Clowe et al.; Lensing Map: NASA/STScI; ESO WFI; Magellan/U.Arizona/D.Clowe et al. Chandra and the Bullet Cluster. NASA Chandra Website, 2013. Released Thursday, October 17th, 2013. Updated Tuesday, October 24th, 2023 at 12:26AM.
- [3] N. Aghanim, Y. Akrami, M. Ashdown, J. Aumont, C. Baccigalupi, M. Ballardini, A. J. Banday, R. B. Barreiro, N. Bartolo, S. Basak, R. Battye, K. Benabed, J.-P. Bernard, M. Bersanelli, P. Bielewicz, J. J. Bock, J. R. Bond, J. Borrill, F. R. Bouchet, F. Boulanger, M. Bucher, C. Burigana, R. C. Butler, E. Calabrese, J.-F. Cardoso, J. Carron, A. Challinor, H. C. Chiang, J. Chluba, L. P. L. Colombo, C. Combet, D. Contreras, B. P. Crill, F. Cuttaia, P. de Bernardis, G. de Zotti, J. Delabrouille, J.-M. Delouis, E. Di Valentino, J. M. Diego, O. Doré, M. Douspis, A. Ducout, X. Dupac, S. Dusini, G. Efstathiou, F. Elsner, T. A. Enßlin, H. K. Eriksen, Y. Fantaye, M. Farhang, J. Fergusson, R. Fernandez-Cobos, F. Finelli, F. Forastieri, M. Frailis, A. A. Fraisse, E. Franceschi, A. Frolov, S. Galeotta, S. Galli, K. Ganga, R. T. Génova-Santos, M. Gerbino, T. Ghosh, J. González-Nuevo, K. M. Górski, S. Gratton, A. Gruppuso, J. E. Gudmundsson, J. Hamann, W. Handley, F. K. Hansen, D. Herranz, S. R. Hildebrandt, E. Hivon, Z. Huang, A. H. Jaffe, W. C. Jones, A. Karakci, E. Keihänen, R. Keskitalo, K. Kiiveri, J. Kim, T. S. Kisner, L. Knox, N. Krachmalnicoff, M. Kunz, H. Kurki-Suonio, G. Lagache, J.-M. Lamarre, A. Lasenby, M. Lattanzi, C. R. Lawrence, M. Le Jeune, P. Lemos, J. Lesgourges, F. Levrier, A. Lewis, M. Liguori, P. B. Lilje, M. Lilley, V. Lindholm, M. López-Caniego, P. M. Lubin, Y.-Z. Ma, J. F. Macías-Pérez, G. Maggio, D. Maino, N. Mandolesi, A. Mangilli, A. Marcos-Caballero, M. Maris, P. G. Martin, M. Martinelli, E. Martínez-González, S. Matarrese, N. Mauri, J. D. McEwen, P. R. Meinhold, A. Melchiorri, A. Mennella, M. Migliaccio, M. Millea, S. Mitra, M.-A. Miville-Deschénes, D. Molinari, L. Montier, G. Morgante, A. Moss, P. Natoli, H. U. Nørgaard-Nielsen, L. Pagano, D. Paoletti, B. Partridge, G. Patanchon, H. V. Peiris, F. Perrotta, V. Pettorino, F. Piacentini, L. Polastri, G. Polenta, J.-L. Puget, J. P. Rachen, M. Reinecke, M. Remazeilles, A. Renzi, G. Rocha, C. Rosset, G. Roudier, J. A. Rubiño-Martín, B. Ruiz-Granados, L. Salvati, M. Sandri, M. Savelainen, D. Scott, E. P. S. Shellard, C. Sirignano, G. Sirri, L. D. Spencer, R. Sunyaev, A.-S. Suur-Uski, J. A. Tauber, D. Tavagnacco, M. Tenti, L. Toffolatti, M. Tomasi, T. Trombetti, L. Valenziano, J. Valiviita, B. Van Tent, L. Vibert, P. Vielva, F. Villa, N. Vittorio, B. D. Wandelt, I. K. Wehus, M. White, S. D. M. White, A. Zacchei, and A. Zonca. *iplanck/i2018 results. Astronomy & Astrophysics*, 641:A6, sep 2020.
- [4] A. Arbey and F. Mahmoudi. Dark matter and the early universe: A review. *Progress in Particle and Nuclear Physics*, 119:103865, July 2021.

- [5] Alexander Bismark. *Simulation and characterization of a LXe TPC for DARWIN RD.* PhD thesis, 12 2019.
- [6] R. Agnese, A. J. Anderson, T. Aramaki, I. Arnquist, W. Baker, D. Barker, R. Basu Thakur, D. A. Bauer, A. Borgland, M. A. Bowles, P. L. Brink, R. Bunker, B. Cabrera, D. O. Caldwell, R. Calkins, C. Cartaro, D. G. Cerdeño, H. Chagani, Y. Chen, J. Cooley, B. Cornell, P. Cushman, M. Daal, P. C. F. Di Stefano, T. Doughty, L. Esteban, S. Fallows, E. Figueroa-Feliciano, M. Fritts, G. Gerbier, M. Ghaith, G. L. Godfrey, S. R. Golwala, J. Hall, H. R. Harris, T. Hofer, D. Holmgren, Z. Hong, E. Hoppe, L. Hsu, M. E. Huber, V. Iyer, D. Jardin, A. Jastram, M. H. Kelsey, A. Kennedy, A. Kubik, N. A. Kurinsky, A. Leder, B. Loer, E. Lopez Asamar, P. Lukens, R. Mahapatra, V. Mandic, N. Mast, N. Mirabolfathi, R. A. Moffatt, J. D. Morales Mendoza, J. L. Orrell, S. M. Oser, K. Page, W. A. Page, R. Partridge, M. Pepin, A. Phipps, S. Poudel, M. Pyle, H. Qiu, W. Rau, P. Redl, A. Reisetter, A. Roberts, A. E. Robinson, H. E. Rogers, T. Saab, B. Sadoulet, J. Sander, K. Schneck, R. W. Schnee, B. Serfass, D. Speller, M. Stein, J. Street, H. A. Tanaka, D. Toback, R. Underwood, A. N. Villano, B. von Krosigk, B. Welliver, J. S. Wilson, D. H. Wright, S. Yellin, J. J. Yen, B. A. Young, X. Zhang, and X. Zhao. Projected sensitivity of the supercdms snolab experiment. *Phys. Rev. D*, 95:082002, Apr 2017.
- [7] J.S. Wilson, H. Meyer zu Theenhausen, B. von Krosigk, E. Azadbakht, R. Bunker, J. Hall, S. Hansen, B. Hines, B. Loer, J.T. Olsen, S.M. Oser, R. Partridge, M. Pyle, J. Sander, B. Serfass, D. Toback, S.L. Watkins, and X. Zhao. The level-1 trigger for the supercdms experiment at snolab. *Journal of Instrumentation*, 17(07):P07010, jul 2022.
- [8] Ritoban Basu Thakur. *The Cryogenic Dark Matter Search Low Ionization-Threshold Experiment.* PhD thesis, University of Illinois at Urbana-Champaign, 2015.
- [9] G. Hinshaw, D. Larson, E. Komatsu, D. N. Spergel, C. L. Bennett, J. Dunkley, M. R. Nolta, M. Halpern, R. S. Hill, N. Odegard, L. Page, K. M. Smith, J. L. Weiland, B. Gold, N. Jarosik, A. Kogut, M. Limon, S. S. Meyer, G. S. Tucker, E. Wollack, and E. L. Wright. Nine-year wilkinson microwave anisotropy probe (wmap) observations: Cosmological parameter results. *The Astrophysical Journal Supplement Series*, 208(2):19, sep 2013.
- [10] F. Zwicky. Die Rotverschiebung von extragalaktischen Nebeln. *Helv. Phys. Acta*, 6:110–127, 1933.
- [11] V. C. Rubin, Jr. Ford, W. K., and N. Thonnard. Extended rotation curves of high-luminosity spiral galaxies. IV. Systematic dynamical properties, Sa - $\text{\`{e}}$ Sc. , 225:L107–L111, November 1978.
- [12] V. C. Rubin, Jr. Ford, W. K., and N. Thonnard. Rotational properties of 21 SC galaxies with a large range of luminosities and radii, from NGC 4605 (R=4kpc) to UGC 2885 (R=122kpc). , 238:471–487, June 1980.
- [13] M. Markevitch, A. H. Gonzalez, D. Clowe, A. Vikhlinin, W. Forman, C. Jones, S. Murray, and W. Tucker. Direct constraints on the dark matter self-interaction cross section from the merging galaxy cluster 1e 0657-56. *The Astrophysical Journal*, 606(2):819–824, may 2004.
- [14] Douglas Clowe, Anthony Gonzalez, and Maxim Markevitch. Weak-lensing mass reconstruction of the interacting cluster 1e 0657-558: Direct evidence for the existence of dark matter. *The Astrophysical Journal*, 604(2):596–603, apr 2004.

Bibliography

- [15] Craig J. Copi, David N. Schramm, and Michael S. Turner. Big-bang nucleosynthesis and the baryon density of the universe. *Science*, 267(5195):192–199, 1995.
- [16] Gianfranco Bertone and Dan Hooper. History of dark matter. *Rev. Mod. Phys.*, 90:045002, Oct 2018.
- [17] Gerard Jungman, Marc Kamionkowski, and Kim Griest. Supersymmetric dark matter. *Physics Reports*, 267(5):195–373, 1996.
- [18] Gianfranco Bertone, Dan Hooper, and Joseph Silk. Particle dark matter: evidence, candidates and constraints. *Physics Reports*, 405(5–6):279–390, January 2005.
- [19] R. Foot and S. Vagnozzi. Dissipative hidden sector dark matter. *Physical Review D*, 91(2), January 2015.
- [20] Marcello Campajola. Dark sector first results at belle ii. *Physica Scripta*, 96(8):084005, May 2021.
- [21] R. Corliss. Searching for a dark photon with darklight. *Nuclear Instruments and Methods in Physics Research Section A: Accelerators, Spectrometers, Detectors and Associated Equipment*, 865:125–127, 2017. Physics and Applications of High Brightness Beams 2016.
- [22] Roberto D. Peccei. *The Strong CP Problem and Axions*, page 3–17. Springer Berlin Heidelberg, 2008.
- [23] R. D. Peccei and Helen R. Quinn. Constraints imposed by CP conservation in the presence of pseudoparticles. *Phys. Rev. D*, 16:1791–1797, Sep 1977.
- [24] Georg G. Raffelt. Astrophysical methods to constrain axions and other novel particle phenomena. , 198(1-2):1–113, December 1990.
- [25] S. J. Asztalos, R. F. Bradley, L. Duffy, C. Hagmann, D. Kinion, D. M. Moltz, L. J. Rosenberg, P. Sikivie, W. Stoeffl, N. S. Sullivan, D. B. Tanner, K. van Bibber, and D. B. Yu. Improved rf cavity search for halo axions. *Phys. Rev. D*, 69:011101, Jan 2004.
- [26] T. Braine, R. Cervantes, N. Crisosto, N. Du, S. Kimes, L. J. Rosenberg, G. Rybka, J. Yang, D. Bowring, A. S. Chou, R. Khatiwada, A. Sonnenschein, W. Wester, G. Carosi, N. Woollett, L. D. Duffy, R. Bradley, C. Boutan, M. Jones, B. H. LaRoque, N. S. Oblath, M. S. Taubman, J. Clarke, A. Dove, A. Eddins, S. R. O’Kelley, S. Nawaz, I. Siddiqi, N. Stevenson, A. Agrawal, A. V. Dixit, J. R. Gleason, S. Jois, P. Sikivie, J. A. Solomon, N. S. Sullivan, D. B. Tanner, E. Lentz, E. J. Daw, J. H. Buckley, P. M. Harrington, E. A. Henriksen, and K. W. Murch. Extended search for the invisible axion with the axion dark matter experiment. *Phys. Rev. Lett.*, 124:101303, Mar 2020.
- [27] N. Du, N. Force, R. Khatiwada, E. Lentz, R. Ottens, L. J Rosenberg, G. Rybka, G. Carosi, N. Woollett, D. Bowring, A. S. Chou, A. Sonnenschein, W. Wester, C. Boutan, N. S. Oblath, R. Bradley, E. J. Daw, A. V. Dixit, J. Clarke, S. R. O’Kelley, N. Crisosto, J. R. Gleason, S. Jois, P. Sikivie, I. Stern, N. S. Sullivan, D. B Tanner, and G. C. Hilton. Search for invisible axion dark matter with the axion dark matter experiment. *Phys. Rev. Lett.*, 120:151301, Apr 2018.
- [28] David J. E. Marsh. Axions and alps: a very short introduction, 2017.

- [29] A. Morales et al. Improved constraints on WIMPs from the international Germanium experiment IGEX. *Phys. Lett. B*, 532:8–14, 2002.
- [30] C. E. Aalseth, P. S. Barbeau, N. S. Bowden, B. Cabrera-Palmer, J. Colaresi, J. I. Collar, S. Dazeley, P. de Lurgio, J. E. Fast, N. Fields, C. H. Greenberg, T. W. Hossbach, M. E. Keillor, J. D. Kephart, M. G. Marino, H. S. Miley, M. L. Miller, J. L. Orrell, D. C. Radford, D. Reyna, O. Tench, T. D. Van Wechel, J. F. Wilkerson, and K. M. Yocom. Results from a search for light-mass dark matter with a p-type point contact germanium detector. *Physical Review Letters*, 106(13), March 2011.
- [31] R. Bernabei, P. Belli, F. Cappella, R. Cerulli, C. J. Dai, A. d’Angelo, H. L. He, A. Incicchitti, H. H. Kuang, J. M. Ma, F. Montecchia, F. Nozzoli, D. Prosperi, X. D. Sheng, and Z. P. Ye. First results from dama/libra and the combined results with dama/nai. *The European Physical Journal C*, 56(3):333–355, August 2008.
- [32] H.S. Lee, H. Bhang, J.H. Choi, I.S. Hahn, D. He, M.J. Hwang, H.J. Kim, S.C. Kim, S.K. Kim, S.Y. Kim, T.Y. Kim, Y.D. Kim, J.W. Kwak, Y.J. Kwon, J. Lee, J.H. Lee, J.I. Lee, M.J. Lee, J. Li, S.S. Myung, H. Park, H.Y. Yang, and J.J. Zhu. First limit on wimp cross section with low background csi(tl) crystal detector. *Physics Letters B*, 633(2–3):201–208, February 2006.
- [33] Dark matter search results from the cdms ii experiment. *Science*, 327(5973):1619–1621, March 2010.
- [34] E. Armengaud. Preliminary results of a wimp search with edelweiss-ii cryogenic detectors, 2010.
- [35] G. Angloher, A. Bento, C. Bucci, L. Canonica, X. Defay, A. Erb, F. von Feilitzsch, N. Ferreira Iachellini, P. Gorla, A. Gütlein, D. Hauff, J. Jochum, M. Kiefer, H. Kluck, H. Kraus, J. C. Lanfranchi, J. Loebell, A. Münster, C. Pagliarone, F. Petricca, W. Potzel, F. Pröbst, F. Reindl, K. Schäffner, J. Schieck, S. Schönert, W. Seidel, L. Stodolsky, C. Strandhagen, R. Strauss, A. Tanzke, H. H. Trinh Thi, C. Türkoğlu, M. Uffinger, A. Ulrich, I. Usherov, S. Wawoczny, M. Willers, M. Wüstrich, and A. Zöller. Results on light dark matter particles with a low-threshold cresst-ii detector. *The European Physical Journal C*, 76(1), January 2016.
- [36] V. N. Lebedenko, H. M. Araújo, E. J. Barnes, A. Bewick, R. Cashmore, V. Chepel, A. Currie, D. Davidge, J. Dawson, T. Durkin, B. Edwards, C. Ghag, M. Horn, A. S. Howard, A. J. Hughes, W. G. Jones, M. Joshi, G. E. Kalmus, A. G. Kovalenko, A. Lindote, I. Liubarsky, M. I. Lopes, R. Lüscher, P. Majewski, A. St. J. Murphy, F. Neves, J. Pinto da Cunha, R. Preece, J. J. Quenby, P. R. Scovell, C. Silva, V. N. Solovov, N. J. T. Smith, P. F. Smith, V. N. Stekhanov, T. J. Sumner, C. Thorne, and R. J. Walker. Results from the first science run of the zeplin-iii dark matter search experiment. *Physical Review D*, 80(5), September 2009.
- [37] E. Aprile, K. Arisaka, F. Arneodo, A. Askin, L. Baudis, A. Behrens, K. Bokeloh, E. Brown, J. M. R. Cardoso, B. Choi, D. B. Cline, S. Fattori, A. D. Ferella, K.-L. Giboni, A. Kish, C. W. Lam, J. Lamblin, R. F. Lang, K. E. Lim, J. A. M. Lopes, T. Marrodán Undagoitia, Y. Mei, A. J. Melgarejo Fernandez, K. Ni, U. Oberlack, S. E. A. Orrigo, E. Pantic, G. Plante, A. C. C. Ribeiro, R. Santorelli, J. M. F. dos Santos, M. Schumann, P. Shagin,

- A. Teymourian, D. Thers, E. Tziaferi, H. Wang, and C. Weinheimer. First dark matter results from the xenon100 experiment. *Physical Review Letters*, 105(13), September 2010.
- [38] D N McKinsey, D Akerib, S Bedikian, A Bernstein, A Bolozdynya, A Bradley, J Chapman, K Clark, T Classen, A Curioni, E Dahl, S Dazeley, M Dragowsky, L de Viveiros, E Druszkiewicz, S Fiorucci, R Gaitskell, C Hall, C Hernandez Faham, L Kastens, K Kazkaz, R Lander, D Leonard, D Malling, R Mannino, D Mei, J Mock, J A Nikkel, P Phelps, T Shutt, W Skulski, P Sorensen, J Spaans, T Stiegler, R Svoboda, M Sweany, M Tripathi, N Walsh, R Webb, J White, F Wolfs, M Woods, and C Zhang. The lux dark matter search. *Journal of Physics: Conference Series*, 203(1):012026, jan 2010.
- [39] R Acciari, M Antonello, B Baibussinov, P Benetti, F Calaprice, E Calligarich, M Cambiaghi, N Canci, C Cao, F Carbonara, F Cavanna, S Centro, M B Ceolin, A Chavarria, A Cocco, F Di Pompeo, G Fiorillo, C Galbiati, L Grandi, B Loer, G Mangano, A Menegolli, G Meng, C Montanari, O Palamara, L Pandola, F Pietropaolo, G L Raselli, M Roncadelli, M Rossella, C Rubbia, R Saldanha, E Segreto, A Szelc, S Ventura, and C Vignoli. The warp experiment. *Journal of Physics: Conference Series*, 308(1):012005, jul 2011.
- [40] S. Archambault, F. Aubin, M. Auger, E. Behnke, B. Beltran, K. Clark, X. Dai, A. Davour, J. Farine, R. Faust, M.-H. Genest, G. Giroux, R. Gornea, C. Krauss, S. Kumaratunga, I. Lawson, C. Leroy, L. Lessard, C. Levy, I. Levine, R. MacDonald, J.-P. Martin, P. Nadeau, A. Noble, M.-C. Piro, S. Pospisil, T. Shepherd, N. Starinski, I. Stekl, C. Storey, U. Wi-choski, and V. Zacek. Dark matter spin-dependent limits for wimp interactions on 19f by picasso. *Physics Letters B*, 682(2):185–192, November 2009.
- [41] E. Behnke, J. Behnke, S. J. Brice, D. Broemmelsiek, J. I. Collar, P. S. Cooper, M. Crisler, C. E. Dahl, D. Fustin, J. Hall, J. H. Hinnefeld, M. Hu, I. Levine, E. Ramberg, T. Shepherd, A. Sonnenschein, and M. Szydagis. Improved limits on spin-dependent wimp-proton interactions from a two liter cf3i bubble chamber. *Physical Review Letters*, 106(2), January 2011.
- [42] Jeffrey Peter Filippini. *Search for WIMP Dark Matter Using the First Five-Tower Run of the Cryogenic Dark Matter Search*. PhD thesis, University of California Berkeley, 2015.
- [43] Nir Ailon, Moses Charikar, and Alantha Newman. Aggregating inconsistent information: ranking and clustering. In *Proceedings of the Thirty-Seventh Annual ACM Symposium on Theory of Computing*, STOC ’05, page 684–693, New York, NY, USA, 2005. Association for Computing Machinery.